ACS OMEGA

http://pubs.acs.org/journal/acsodf

Article

Sugar-Based Phase-Selective Supramolecular Self-Assembly System for Dye Removal and Selective Detection of Cu^{2+} Ions

Panichiyil Valiyaveetil Bhavya, Kamalakannan Soundarajan, Jan Grzegorz Malecki, and Thangamuthu Mohan Das*

Cite This: *ACS Omega* 2022, 7, 39310−39324

Read Online

ACCESS | Metrics & More | Article Recommendations | Supporting Information

ABSTRACT: Simple, effective, and eco-friendly sugar-based phase-selective gelators were synthesized at a low cost. They showed high gelling ability toward a wide range of solvents at lower concentrations (minimum gelation concentration ∼0.3%). Preliminary tests reveal that these low molecular weight organogelators can immediately and phase-selectively gel benzene, toluene, petrol, and kerosene in water at room temperature. We also identified G13 in toluene as the good gelator, and the corresponding organogel proficiently removes water-soluble dyes from their concentrated aqueous solutions. This efficient removal of toxic organic solvents and dyes from water suggests promising applications in removing organic substances from contaminated water resources. The thermoreversible gel exhibits effective rechargeability up to five cycles of burning and gelation, which imply the flame stability of the gel. Interestingly, these compounds had a high detection ability toward Cu^{2+} ions with a state change from gel to the solution. The physical justification for gelation mechanisms and the molecular interaction with metal ions were further confirmed by computational studies.

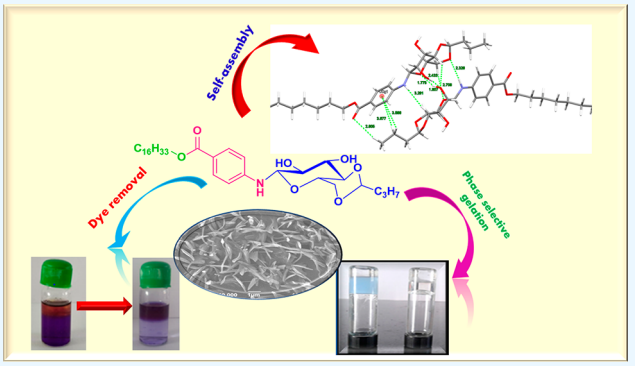

INTRODUCTION

Low molecular weight organogelators (LMOGs)[1,2] have received substantial attention in recent decades due to their wide range of potential applications in various fields,[3] such as drug delivery,[4−6] sensing,[7,8] oil spill recovery,[9−11] water purification,[12] and dye absorption.[13,14] The formation of LMOGs is generally due to the noncovalent forces such as hydrogen bonding, van der Waals, electrostatic, hydrophobic, and $\pi-\pi$ stacking interactions.[15] The organogels formed via the self-aggregation of small gelator molecules are called supramolecular organogelators.[16,17] They can sensitively respond to several external stimuli,[18−20] such as light, heat, pressure, magnetism, pH, mechanical force, ultrasound, and chemical substances. A disturbance of the weak points by external stimuli may disrupt the gel to the sol state. Such a phase transformation in the presence of an analyte is a good approach for developing new sensor devices for naked-eye detection of biologically relevant metal ions.[21,22]

Self-assembly of sugar-derived low molecular weight gelators has become a remarkable research topic. Due to the presence of free hydroxyl groups, they use hydrogen bonding for their self-assembly process. Since carbohydrates are biocompatible, biodegradable, rich in stereochemistry, nontoxic, eco-friendly, inexpensive, and moreover derived from abundant renewable resources, they have proven to be an ideal choice for the development of organogels compared with other gel types.[23] Carbohydrate-derived organogelators display applications in various fields, such as oil-spill recovery, semiconducting fabrics, CO_2 absorption, generation of nanocomposite materials, soft-optical devices, separating biomolecules, lectin binding, controlled drug encapsulation, release and delivery, self-healing, metal ion detection, and many others.[24−26]

A fascinating category of supramolecular gelators is the phase-selective organogelators (PSOGs) which preferentially gelate organic solvent over others from a given biphasic system consisting of both aqueous and nonaqueous solvent mixtures at room temperature.[27,28] This remarkable feature of PSOGs allows them to remove organic solvents and dyes from contaminated water by solidifying oil spills and dyes. Though dyes are used as coloring agents in several industries for coloring their products, they are toxic and their direct discharge into the water sources is harmful to human and aquatic lives. Therefore, there is always a need for an effective dye adsorbent system. Usually, photocatalytic degradation,[29−31] photoelectrocatalytic degradation,[32] photodegrada-

Received: August 25, 2022
Accepted: October 6, 2022
Published: October 18, 2022

tion,[33,34] photo-Fenton catalytic degradation,[35,36] Janus nano-absorbents,[37] nanocomposites,[38,39] activated carbon,[40,41] and biosorption methods[42−44] have been used to remove organic contaminants such as dyes and harmful chemicals from wastewater. However, phase-selective supramolecular organo-gelators having appropriate hydrophilic/hydrophobic sites are usually found to be promising in this process. The first reported PSOGs were amino acid-based amphiphiles synthe-sized by Bhattacharya and co-workers in 2001.[45] For a molecule to become an excellent PSOG, there are some essential requirements: (i) the gelator molecule should gelate the oil/dye efficiently and instantly from the biphasic mixture at room temperature; (ii) there should be easy recovery of the oil/dye from the gel phase; (iii) a reusable gelator should be generated; (iv) the production cost should be low.

The recognition and sensing of environmentally and biologically essential transition metal ions have drawn great concern in the area of supramolecular chemistry.[46,47] Among the different metal ions, copper is a vital trace element in the human body, playing a crucial role in many fundamental physiological processes in living organisms. However, its deficiency and excess are harmful to human health.[48,49] High Cu^{2+} concentrations cause oxidative stress and disorders, such as Alzheimer's, Wilson's, and Menke's diseases.[50] Hence, an easy and effective method for the detection of Cu^{2+} ions, predominantly in a sol−gel medium, is desirable.

The development of PSOGs to efficiently remove aromatic compounds and dyes is still of strong interest in material science. Based on these particular applications, eco-friendly low molecular weight phase-selective sugar-based organogelators have been developed and their gelation behavior has been studied in various solvents, fuel oils, and a mixture of solvents. These gelators also exhibit selective sensing of Cu^{2+} ions in the gel state via gel−sol phase transformation. To support our experimental findings, we corroborated our experimental results with DFT calculations. The gelators presented in this work are designed to have long alkyl chains and aromatic structures, which form gels rapidly in most of the aliphatic as well as aromatic solvents. They could serve as a highly efficient agent to remove oil spills and water-soluble dyes to purify polluted water in a practical situation.

RESULTS AND DISCUSSION

O-Alkylaminobenzoate-based *N*-glycosylamines (**G8−G13**) were synthesized from 4-nitrobenzoyl chloride (**1**) by adopting the literature procedure (please refer to the Supporting Information).[51] *N*-Glysylamines of *O*-alkylaminobenzoates (**G8−G13**) were synthesized from *O*-alkylaminobenzoate derivatives **5−7** and 4,6-O-protected D-glucose (**a−c**) (Scheme 1) in good yield. All of the new *O*-alkylaminobenzoate-based *N*-glycosylamine derivatives (**G8−G13**) were identified through different spectral techniques.

The formation of alkyl 4-aminobenzoate was confirmed by nuclear magnetic resonance (NMR), high-resolution mass spectrometry (HR-MS), and Fourier transform infrared (FT-IR) techniques (details are provided in the Supporting Information). The final compounds, **G8−G13** were confirmed by ^{1}H and ^{13}C NMR spectroscopy. From the ^{1}H NMR, the presence of the alkyl chain was confirmed from the peaks that appeared in the range of 0.60−2.56 ppm. The sugar skeletal protons resonate around 3.04−6.05 ppm, and the existence of the β-anomeric form of the glycosidic unit was confirmed from the triplet appearing in the region of 3.57−5.07 ppm with a coupling constant of 6.0−9.0 Hz. The ^{13}C NMR analysis of the compounds (**G8−G13**) shows peaks in the range of 13.4−64.1 and 102.6−65.8 ppm corresponding to the aliphatic carbon and the skeletal sugar carbon. This supports the formation of the predicted product.

Scheme 1. Synthesis of Alkyl-Substituted *N*-Glycosylamines (G8−G13)

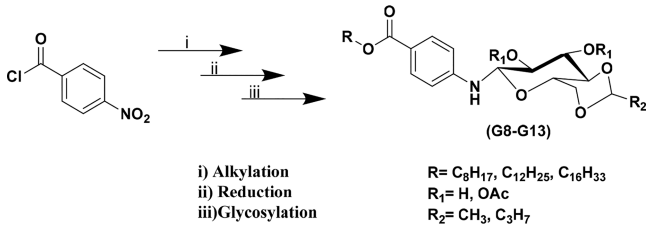

Broad Spectrum of Gelling Abilities. The gelation ability of six different *O*-alkyl benzoate-based *N*-glycosylamine derivatives was tested in 15 polar and nonpolar organic solvents, and the results are summarized in Table 1. Compounds **G11**, **G12**, and **G13** showed excellent ability to gelate different aliphatic and aromatic solvents, and these gels were found to be sturdy at room temperature for more than 1 month (Figure 1).

Protecting groups such as ethylidene and butylidene in the D-glucose moiety showed a notable change in the gelation process. In this series of compounds, the *N*-glycosylamine, **G13**, could gelate at a CGC of 0.3%. The gelation ability of organogelators significantly depends on the gelator−gelator and solvent−gelator interactions, which involve both specific and nonspecific intermolecular forces (H-bonding, dipole−dipole, dipole-induced, and instantaneous dipole-induced forces (also termed as dispersion forces)). We believe that the hydroxyl group on the glucose moiety is crucial for gel formation because it allows participation in intermolecular hydrogen bonding. In addition to that, the $\pi-\pi$ stacking interaction of the benzene ring and hydrogen bonding of the −NH proton is also supportive for gel formation. These gels exhibit good thermal reversibility with a gel−sol transition temperature.

In addition, all of the gelators showed high selectivity for the gelation of organic phases in biphasic systems consisting of water and aromatic solvents and oils. To study this property, a phase-selective gelation experiment was conducted (Figure 2).

Gelator **G13** (0.3%) shows excellent phase selectivity when placed in the mixture of water and organic solvents and can be employed as an effective and recyclable PSOG to simplify the separation of aromatic solvents from aqueous phases in biphasic systems. The organic layer was selectively gelled even when a large volume of water is present.[52] The alkyl-substituted aminobenzoate-based *N*-glycosylamine selectively gelates benzene, kerosene, and petrol, which supports the ability of the synthesized gelators to remove the liquid petroleum hydrocarbon from contaminated water (Scheme S1).

Flame Stability. Interestingly, gelator **G13** showed impressive stability against higher temperatures in almost all alcoholic solvents, hence these gels can be used as safe fuels. A small piece of the gel of gelator **G13** in ethanol was set on fire with a matchstick. The gel did not produce any smoke, unpleasant odor, ash, or shoot on burning. Once burnt, the residue was taken into ethanol, and we could reverse the

https://doi.org/10.1021/acsomega.2c05466
ACS Omega 2022, 7, 39310−39324

Table 1. Gelation Studies of *O*-alkyl Benzoate-Based *N*-Glycosylamines (G8−G13)[a]

	compounds (CGC%)					
solvents	G8	G9	G10	G11	G12	G13
hexane	PG	PG	IS	G(0.9)	G(0.9)	G(0.9)
cyclohexane	PG	G(0.8)	S	G(0.8)	G(0.6)	G(0.6)
ethyl acetate	S	S	S	S	S	S
chloroform	PG	PG	PG	PG	PG	PG
1,2-dichloroethane	S	S	S	S	S	S
ethanol	G(0.7)	G(0.7)	S	G(0.6)	G(0.5)	G(0.5)
water	I	I	I	I	I	I
DMF	S	S	S	S	S	S
DMSO	S	S	S	S	S	S
methanol	PG	PG	S	PG	PG	PG
toluene	G(0.5)	G(0.5)	S	G(0.4)	G(0.3)	G(0.3)
1,2-dichlorobenzene	G(0.6)	G(0.5)	S	G(0.5)	G(0.4)	G(0.3)
benzene	G(0.7)	G(0.7)	S	G(0.6)	G(0.5)	G(0.3)
petrol	G(0.6)	G(0.5)	S	G(0.6)	G(0.5)	G(0.50
kerosene	G(0.6)	G(0.6)	S	G(0.4)	G(0.4)	G(0.3)

[a]I, S, PG, and G denote insoluble, soluble, partial gel, and gel, respectively.

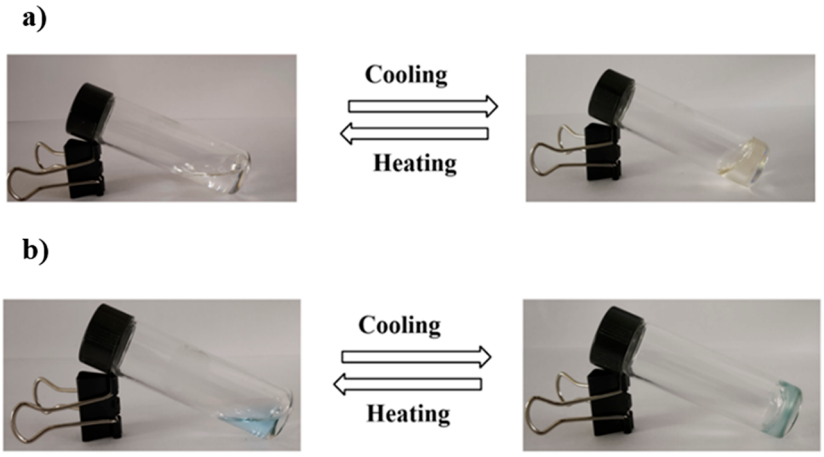

Figure 1. Photograph showing the solution to gel transformation of compound **G13** (CGC 0.3%): (a) gel derived from benzene and (b) gel derived from kerosene.

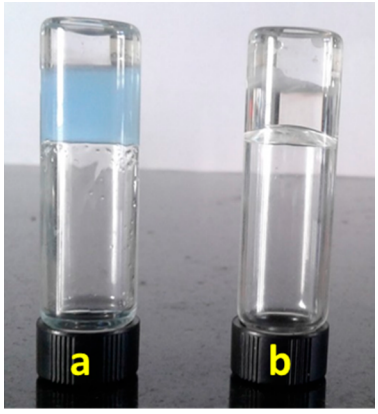

Figure 2. Photographs showing phase selective gelation of gelator **G13** in (a) kerosene−water and (b) benzene−water.

gelation successfully (Figure S2). The cycle of burning and regenerating the gel was repeated five times to confirm that the gelator holds the steady memory of the supramolecular architecture even after burning and can be reused several times by just adding alcohols at a particular proportion.[53]

Determination of Gel−Sol Transition Temperature. The gel−sol transition temperature (T_{gs}) was determined by placing the organogel-containing screw-capped glass vial (i.d. = 10 mm) into a thermostated oil bath, and it was gradually heated and the temperature observed. The temperature at which the gel melted to the solution was recorded as T_{gs}. Above the melting point, the gel converts to the solution, and upon cooling below T_{gs}, it forms the gel (Figure S3). The gelation processes are thermoreversible; that is, they can be transformed to the solution above a specific temperature (T_{gs}) and be reformed upon cooling. The gelation abilities remain intact even after several repetitions of the sol−gel cycle, proving the thermoreversible nature of the gels. Upon increasing the concentration of the gelator, the T_{gs} value increases, which designates the stability enhancement of the gel at high gelator concentrations. In the gel state, the gels form aggregates, whereas in the sol phase, the aggregates are dissociated into discrete molecules of the gelator.[54]

Organogel Morphology. To obtain visual insights into the self-assembly, dry samples of organogels have been prepared at the concentration of their respective CGC and were subjected to field-emission scanning electron microscopy (FE-SEM). Low molecular weight organogels can be self-

https://doi.org/10.1021/acsomega.2c05466
ACS Omega 2022, 7, 39310−39324

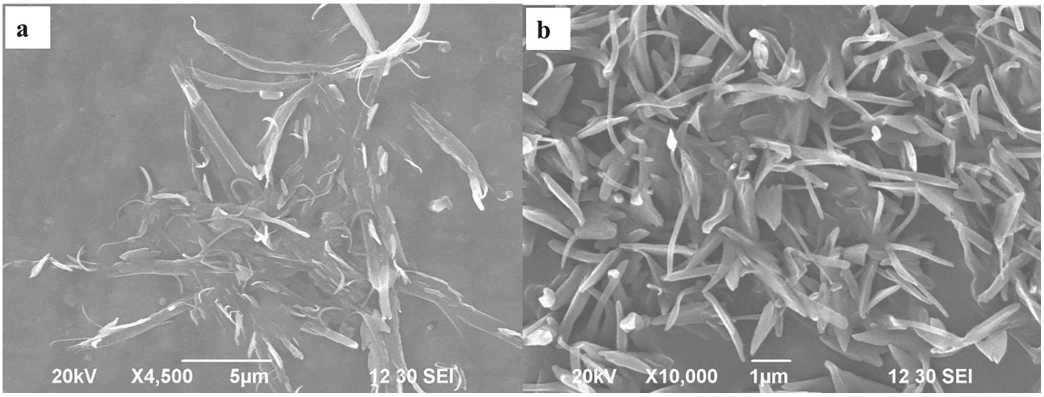

Figure 3. FE-SEM images of compound **G13** in benzene with different magnification: (a) 5 μm and (b) 1 μm.

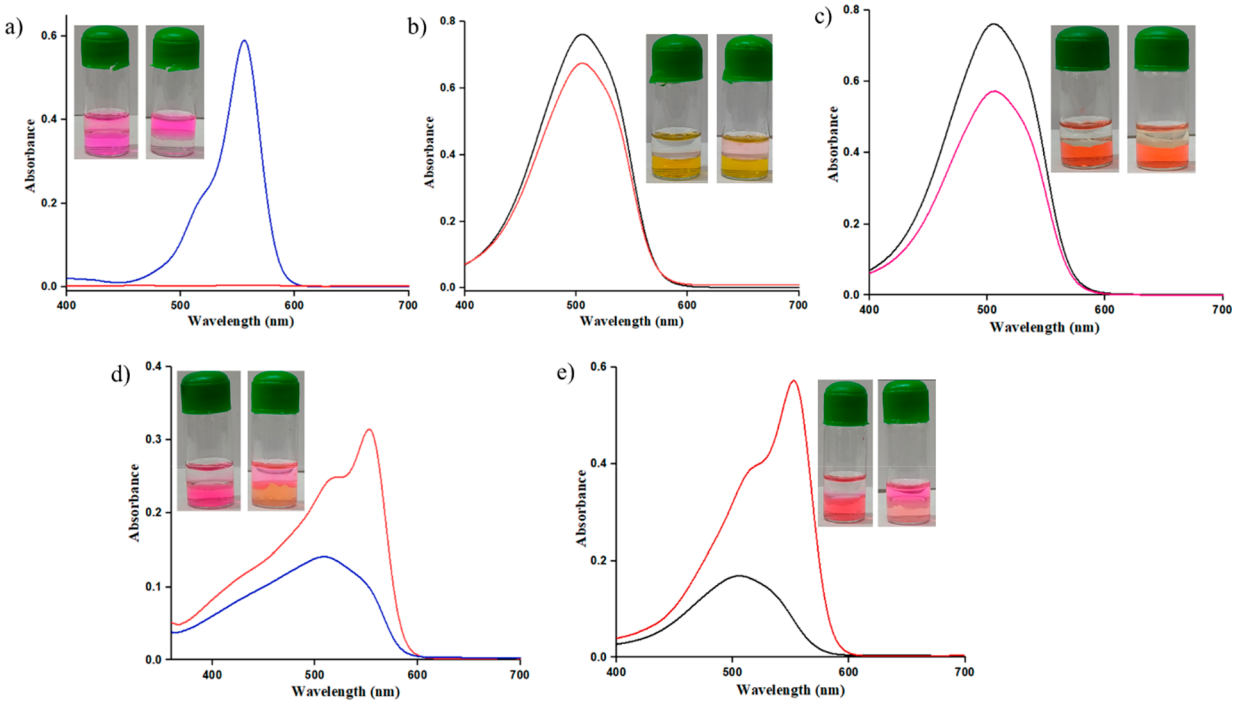

Figure 4. Change in absorbance of (a) Rhodamine B (RhB), (b) Crystal Red (CR), Methyl Orange (MO), (c,d) RhB/MO mixture (1:1, v/v), and (e) RhB/CR mixture (1:1, v/v) by the benzene gel of **G13** (0.4%) ([dye] = 3.5×10^{-5} M).

assembled under the driving force of the noncovalent interaction. FE-SEM images of compound **G13** in benzene exhibited a fibrous 3D network pattern (Figure 3).

Dye Removal. One of the emerging research fields is developing robust methods to remove toxic dyes from contaminated water. Our preliminary findings show that the synthesized gelators can act as a PSOG for extracting aromatic compounds from water. It is thus expected that the self-assembled three-dimensional networks of organogels could entrap and arrest the toxic dye molecules from water by forming gels.[55,56] It was observed that the gel obtained from **G13** selectively absorbs cationic toxic dyes such as Crystal Violet (CV) and Rhodamine B (RhB) from the water with 98% removal efficiency within 24 h (calculated from UV−vis absorption curves, Figure S4). Moreover, further experiments showed that these gels can selectively remove cationic dyes from a mixture of cationic and anionic dyes from water (Figure 4).

To check the feasibility of pollutant dye removal, a 0.4% gel of gelator **G13** in benzene was added to the surface of an aqueous 3 mL solution of CV dye. The solution was stored at room temperature without any turbulence. Attractively, it was observed that the aqueous layer gradually started fading (Figure 5a−d). The UV/vis absorption spectra of the aqueous CV dye solution (it exhibits a maximum absorption wavelength at 587 nm) at different time intervals are shown in Figure S6 (please refer to the Supporting Information). Figure 5e shows the absorption spectra of CV dye in aqueous solution before and after the treatment with **G13** PSOG, and the absorptivity is estimated to be 97.50%, calculated from eq 1 (please refer to the Supporting Information).[57] All of the newly synthesized gelators were tested for dye removal, and the results are tabulated in Tables S1 and S2 (please refer to the Supporting Information). It can be speculated that the hydrophobic interaction between the aromatic moieties in the gelators and the dye molecules is the key driving force for dye adsorption. Upon increasing the alkyl chain length of the gelator molecule,

https://doi.org/10.1021/acsomega.2c05466
ACS Omega 2022, 7, 39310−39324

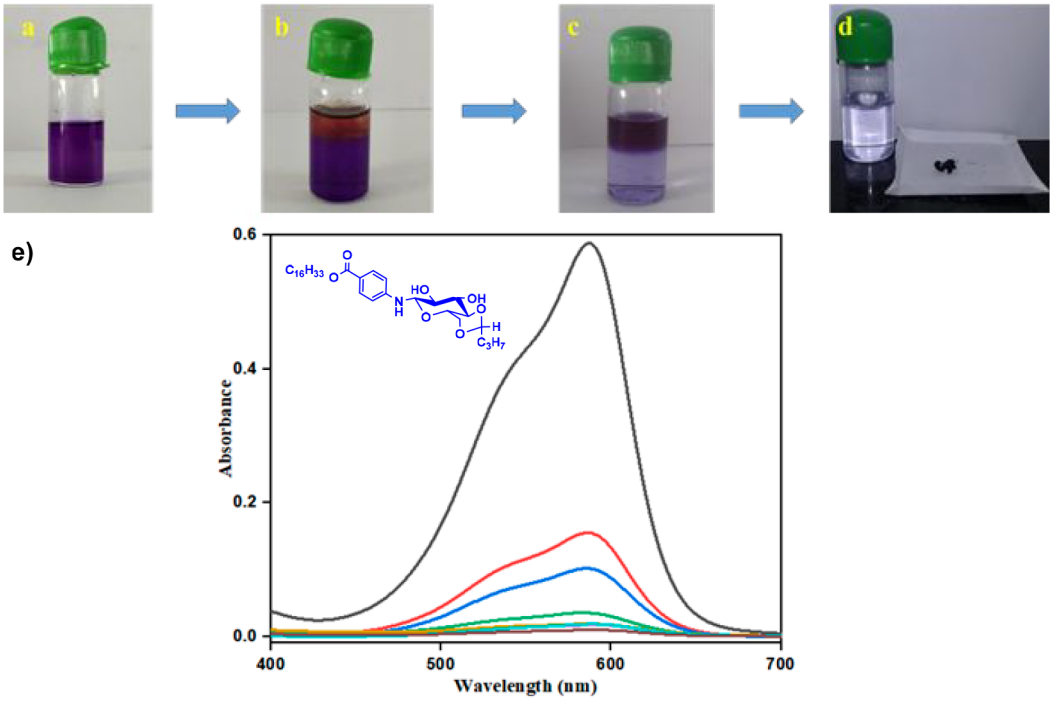

Figure 5. Photographs of CV dye absorption studies of compound **G13**: (a) CV dye in water, (b) CV dye solution along with gel, (c) after 24 h, and (d) extracted gel (xerogel) from the water, and (e) absorption spectra of **G13** in water contaminated with CV dye at different time intervals (0−24 h).

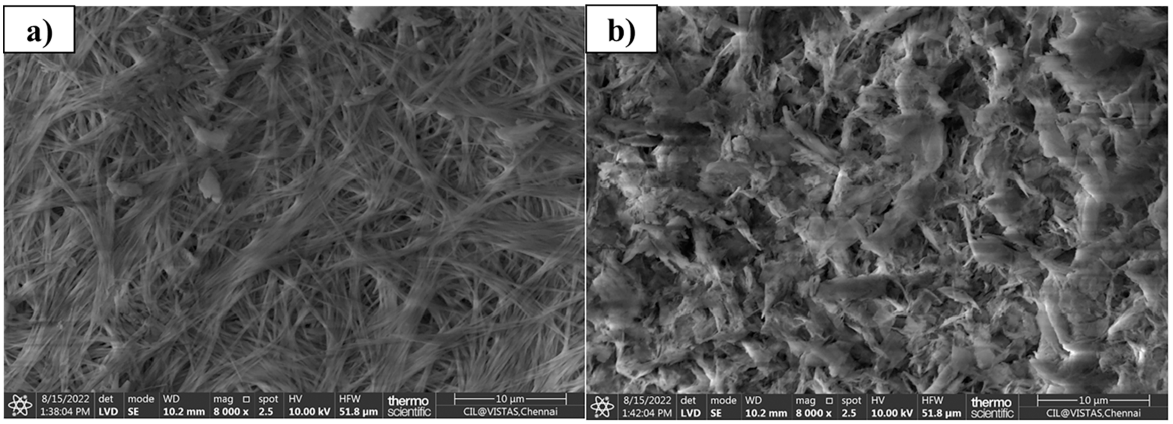

Figure 6. FE-SEM images of compound **G13** (a) before and (b) after the removal of the dye.

the dye removal efficiency increased (Tables S1 and S2). The existence of both the hydrophilic hydroxyl head and the hydrophobic alkyl chains in the compound structure is highly advantageous for accommodating organic dyes out of the water (a schematic diagram of the mechanism for the removal of dye has been given in Figure S5). In addition, the large surface area of the self-assembled fibrous network is a critical factor for entrapping the dye molecules with high efficiency. Recycling of the gelator was carried out using methanol as a solvent, and the recovered gelator was further used to remove the dye five times, as shown in Figure S7. From the bar diagram, it has been found that the dye removal capability of the gelator decreases slightly in each adsorption−desorption process (see the Supporting Information for more details).

The FE-SEM images of gelator **G13** before and after the removal of the dye were recorded and are shown in Figure 6. After removal of the dye, the morphology of the gelator was changed from a fibrous pattern to a flake-like pattern. We assume that during the dye removal process a small amount of dye has been entrapped in the gelator; therefore, the removal efficiency decreases during each cycle, and it causes changes in morphology. This result demonstrated that the gelator has very good recyclability for dye removal and can be used as a good contender for water purification. Moreover, it is easy to use, reusable, and can be applied to the large-scale treatment of wastewater.

Adsorption Kinetics and Thermodynamics Studies. Adsorption studies of CV dye onto the gels were analyzed by applying pseudo-first-order and second-order models and also Langmuir and Freundlich isotherms.[58] Figure 7a,b shows the plots for the two different adsorption kinetic models, and the constant values are calculated and summarized in Table S3 (please refer to the Supporting Information). The pseudo-first-order adsorption kinetics assumes that the dye adsorption rate

https://doi.org/10.1021/acsomega.2c05466
ACS Omega 2022, 7, 39310−39324

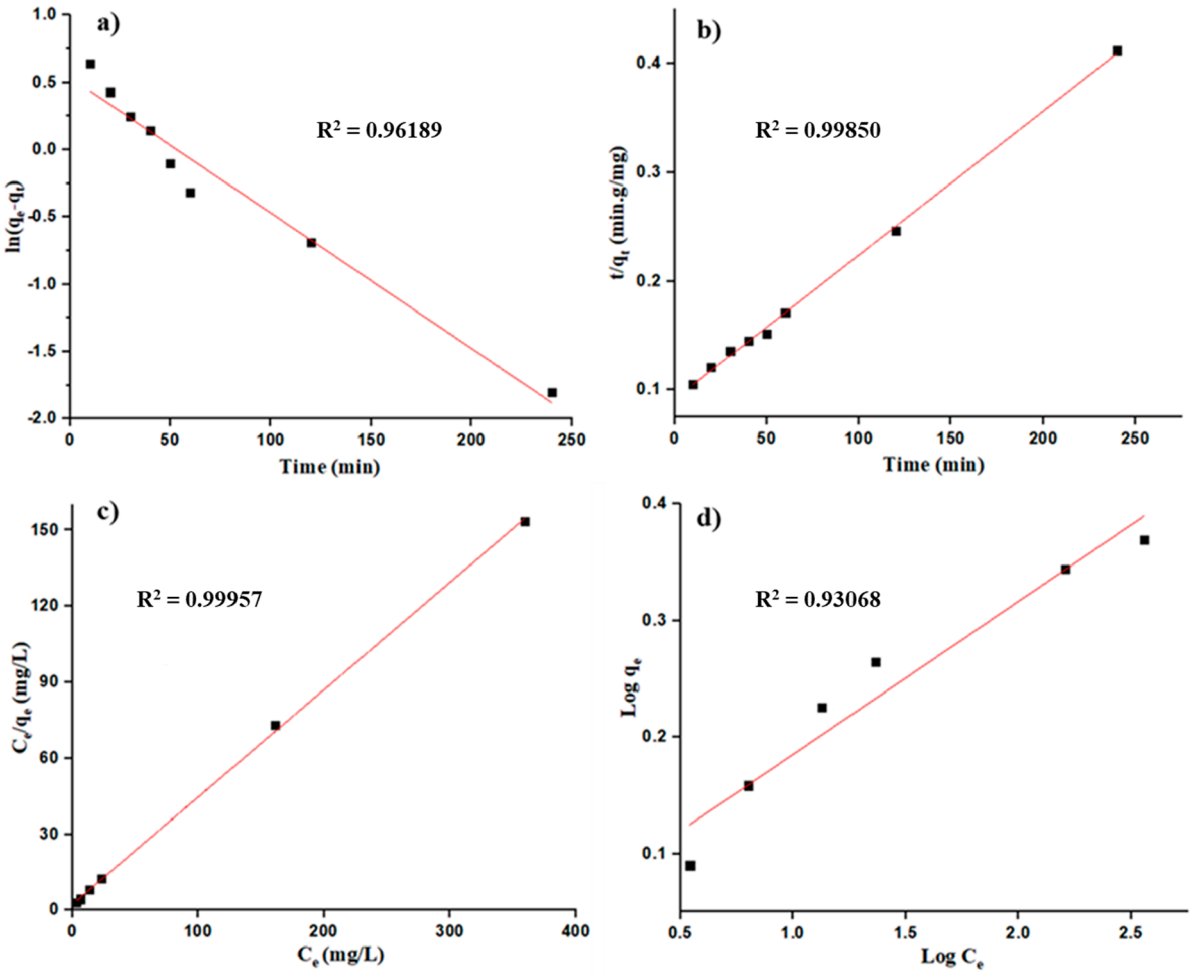

Figure 7. (a) Pseudo-first-order adsorption kinetics, (b) pseudo-second-order adsorption kinetics, (c) Langmuir adsorption isotherm, and (d) Freundlich adsorption isotherm.

is directly proportional to the number of unoccupied sites. However, the equation is not well fitted, and the calculated value of the equilibrium adsorption capacity is quite different from the experimental value. The correlation coefficient (R^2) of the pseudo-second-order adsorption kinetic equation of **G13** is larger than 0.98, but the value of the equilibrium adsorption capacity of the pseudo-first-order is not in good agreement with the experimental value. This result shows that the pseudo-first-order model was not suitable for fitting the adsorption of dyes.

The adsorption isotherms show the relationship between the adsorbate concentration after the equilibrium between solid and liquid phases, which can be used to characterize the adsorption capacity of gel for CV dye. Figure 7c,d and Table S4 (please refer to the Supporting Information) show that the Langmuir adsorption isotherm is more suitable than the Freundlich adsorption isotherm. The calculated value of equilibrium adsorption capacity is close to the experimental value. The R^2 value close to 1 (0.9995) and small deviation between calculated q (24.4 mg/g) and experimental q (23.4 mg/g) indicated that monolayer adsorption occurs on the adsorbent surface with identical homogeneous sites.

Effect of Contact Time on Adsorption of CV Dye. The effect of contact time on the adsorption capacity of **G13** for CV dye, Q, is given in Figure 8. The result shows that, as contact time increases from 1 to 36 h, the adsorption capacity

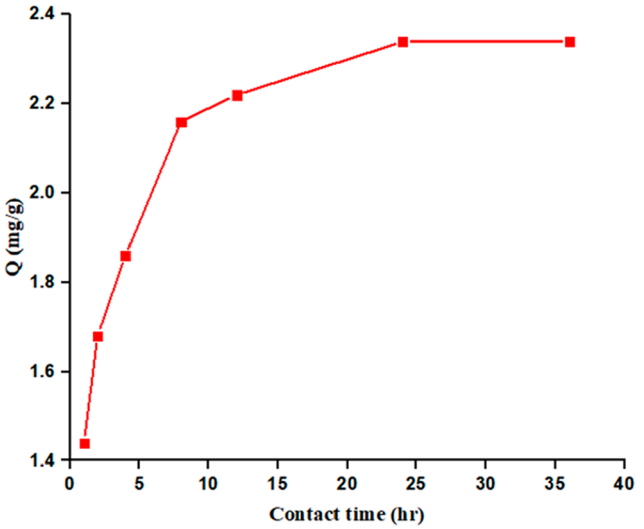

Figure 8. Effect of contact time on the adsorption of CV dye onto the gel derived from **G13** in benzene.

sharply increased from 1.44 mg/g (1 h) to 2.18 mg/g (8 h) and, after that, only increased sluggishly and remained stable around 2.34 mg/g from 12 to 36 h. Based on the result, rapid uptake of CV dye by **G13** happens during early contact time due to an abundance of adsorption sites on the gel surface.

https://doi.org/10.1021/acsomega.2c05466
ACS Omega 2022, 7, 39310−39324

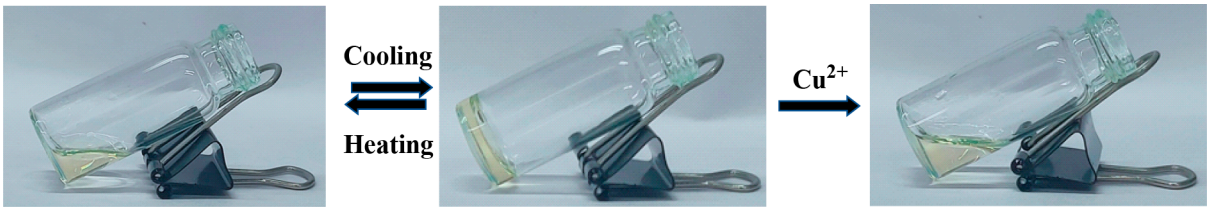

Figure 9. Photograph of the solution to gel transformation of **G13** and Cu^{2+}-induced conversion of gel to the solution (toluene, 0.3%).

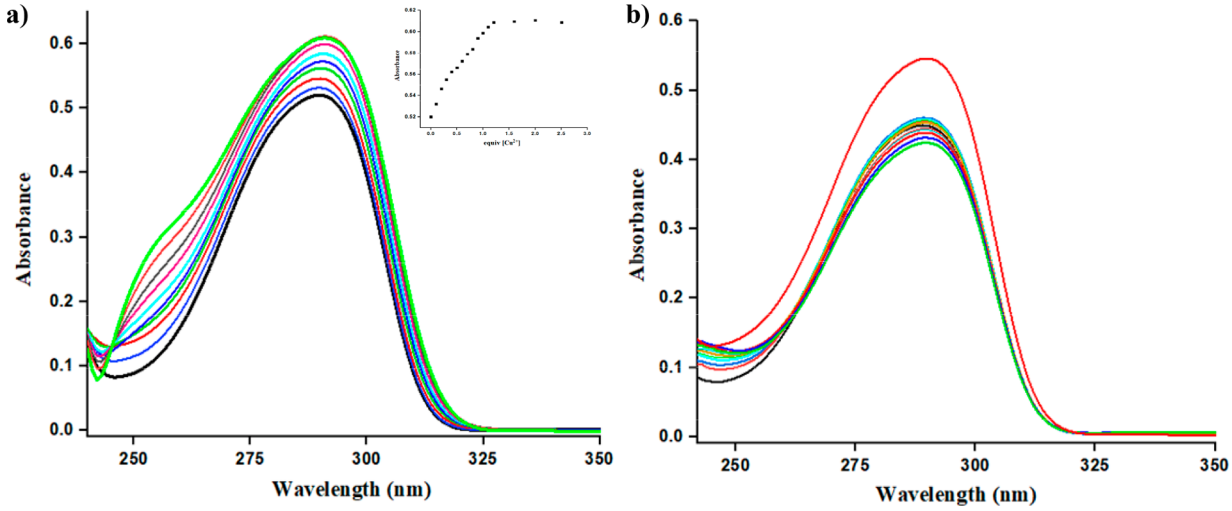

Figure 10. (a) Change in absorbance of **G13** (c = 10 μM) upon addition of 0−2.5 equiv of Cu^{2+} (c = 1.0 × 10^{-5} M). Inset: UV−vis absorption spectral changes during titration of **G13** (10 μM) with 0−2.5 equiv of Cu^{2+} at 290. (b) Change in absorbance of **G13** upon gradual addition of all metals (c = 1.0 × 10^{-5} M) in EtOH−H_2O (2:1, v/v).

Metal Ion Responsive Behavior in the Gel State. The metal ion responsiveness of the gel was studied by adding ethanolic solutions of metal ions (Ba^{2+}, Fe^{3+}, Co^{2+}, Ni^{2+}, Zn^{2+}, Cu^{2+}, Mn^{2+}, Cd^{2+}, Ca^{2+}, Mg^{2+}, Hg^{2+}, Pb^{2+}; all were used as nitrate salts (c = 0.05 M)) to the toluene gel of **G13** (0.3% w/v). Among the different metal ions, only Cu^{2+} disrupted the gel to the sol immediately after being shaken (Figure 9). A minimum of 0.3 equiv of Cu^{2+} was adequate to induce the gel-to-sol transformation, and it took only about 1 min for complete disruption of the gel. We believe that the −NH groups which are involved in the coordination of Cu^{2+} rupture the aggregation.

Metal Ion Interaction in Solution. Absorption titration of **G13** (c = 10 μM) was carried out with different metal ions (nitrate salts of Ba^{2+}, Fe^{3+}, Co^{2+}, Ni^{2+}, Zn^{2+}, Cu^{2+}, Mn^{2+}, Cd^{2+}, Ca^{2+}, Mg^{2+}, Hg^{2+}, and Pb^{2+}) in EtOH−H_2O (9:1, 10 mL) mixture. An absorbance band at 290 nm was observed in the spectrum of **G13**. With the addition of Cu^{2+} to **G13**, the absorption intensity of the peak at 290 nm was increased gradually, but the addition of other metal ions to **G13** induced a negligible absorption change. These results suggest that G13 has a good selectivity to Cu^{2+} ions (Figure 10a,b).

A competitive experiment was performed by adding 10 μM Cu^{2+} to the solution of **G13** (20 μM) in the presence of an equimolar concentration of various metal ions including Ba^{2+}, Fe^{3+}, Co^{2+}, Ni^{2+}, Zn^{2+}, Cu^{2+}, Mn^{2+}, Cd^{2+}, Ca^{2+}, Mg^{2+}, Hg^{2+}, and Pb^{2+}. As depicted in Figure S8a (please refer to the Supporting Information), except for Cu^{2+}, other competitive metal ions did not produce a significant absorption change. Upon addition of Cu^{2+} to the solution of **G13** in the presence of other metal ions, a significant increase in absorption at about 290 nm is noticed. These results reveal that the recognition of Cu^{2+} by **G13** is not influenced by other competitive metal ions (Figure S8b; refer to the Supporting Information).

To confirm the binding sites of sensor responses of **G13**, the stoichiometry of **G13** + Cu^{2+} was calculated through Job's plot, as shown in Figure S9 (refer to the Supporting Information). The stoichiometry of **G13** was established by Job's plot between the mole fraction and relative intensity changes at 290 nm. The absorbance at 290 nm obtained a maximum when the molar fraction was 0.70, which suggests a 1:2 stoichiometry for the Cu^{2+}−**G13** complex. We examined the reversibility of the sensor using disodium salt of ethylenediaminetetraacetic acid (Na_2EDTA). The addition of Cu^{2+} to **G13** resulted in an increase in the absorbance intensity at 290 nm, indicating the binding of the metal ion (Figure S10; refer to the Supporting Information). The addition of Na_2EDTA to a mixture of **G13** and Cu^{2+} resulted in a decrease in the absorbance intensity at 290 nm, indicating the regeneration of the free **G13**. The absorbance intensity was recovered by the addition of Cu^{2+} again. This makes the molecule reusable and interesting for real-time applications to sense Cu^{2+} ions. The detection limits of **G13** toward Cu^{2+} were determined through UV−vis titration (limit of detection = 6.96 μM). The calibration curves for the determination of detection limits are given in the Supporting Information (Figure S11). The **G13** sensor was compared with the reported Cu^{2+} chemosensor in the literature, as shown in Table S5. Our sensor **G13** is more advantageous than the reported chemosensor of Cu^{2+}.

Computational Studies. Nowadays, material characterization methods under a big data environment and several diseases such as Parkinson's disease, cardiovascular disease, or

https://doi.org/10.1021/acsomega.2c05466
ACS Omega 2022, 7, 39310−39324

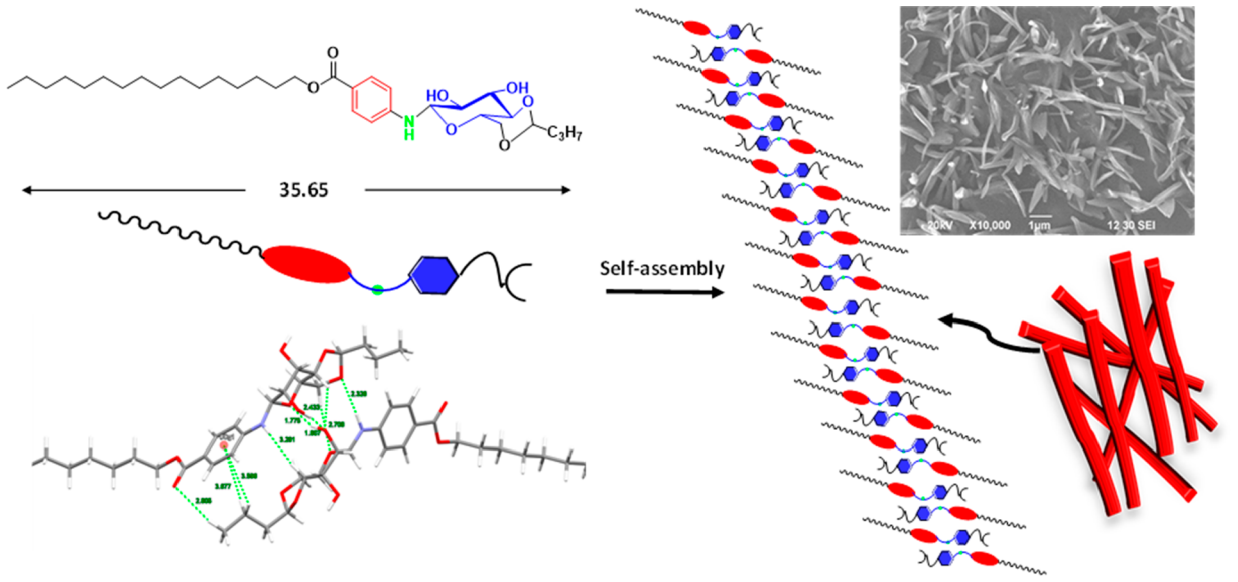

Figure 11. Molecular structure, molecular model, aggregate model, and morphologies of the xerogel of **G13**.

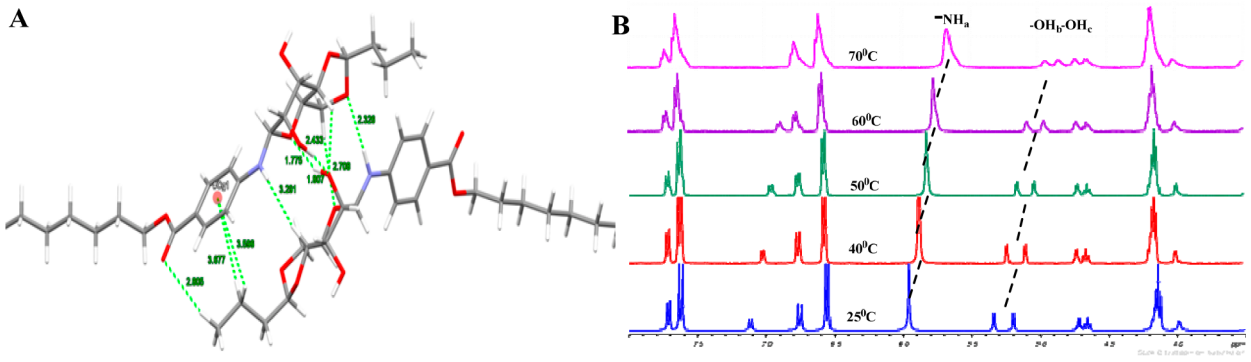

Figure 12. (A) Optimized geometry of **G13** dimer. (B) Partial ^{1}H NMR spectra of 15 mg of **G13** in 0.6 mL of DMSO-d_6 as the temperature increased from 25 to 70 °C.

coronavirus infection have been analyzed by making use of machine learning through artificial intelligence.[59,60] Similarly, by implementing computational science and making use of mathematical models, one can solve any scientific problems easily and also can prove or support an experimental result.[61] Using DFT calculations, some of our experimental findings have also been investigated by computational methods. Compound **G13** is characterized by the largest linear dimensions, obviously related to the length of the alkyl chain (Figure S12), which is important for the van der Waals interactions between the gelator molecules leading to the formation of a three-dimensional gel structure. To have an insight into the association model of the molecules, the geometry of dimers was optimized. Based on the DFT calculations, a possible self-assembly mechanism for the two-component gelators was proposed, as shown in Figure 11. We assume **G13** molecules appeared to exhibit two types of intermolecular interactions: (1) interactions between hydroxyl groups and ring oxygen of glucose and (2) van der Waals forces between alkyl chains. The primary intermolecular interaction for **G13** was an expected polar (i.e., hydrogen bonding) interaction between the −OH and the −NH groups with a nearby ring oxygen. Illustrations of representative dimer interactions are found in Figures S13.

To quantify the magnitude of intermolecular interactions between molecules within the gel, the energies of the monomer and dimer were calculated using the counterpoise method of Boys and Bernardi.[62] The effect of counterpoise correction (basis set superposition error) on the geometries was taken into account. The correction is applied to recalculate the binding energy of the dimer. The highest interaction energy (ΔE = −31.50 kcal/mol) occurs when the molecules are arranged parallelly, as shown in Figure 12A. Hydrogen bonds and C−H···π stacking interactions play a significant role in this configuration. The values of calculated interaction energies of **G10**−**G13** dimers are equal to −28.48, −26.91, −20.66, and −31.28 kcal/mol, respectively. The hydrogen bonding in gel formation was also confirmed by the upshifted signals of $-NH_a$ and $-OH_b$ and $-OH_c$ protons from 5.96, 5.34, and 5.20 ppm to 5.66, 4.94, and 4.64 ppm as the temperature increased from 25 to 70 °C in ^{1}H NMR spectroscopic analysis (Figure 12B). The set of hydrogen bonds significantly affects the stability of the gel. On the other hand, the impact of π-stacking interactions is relatively small, which can be deduced from the calculated energy value shown in Figure S13C (refer to the Supporting Information).

From the molecular conformation and electrostatic potential map in Figure 13, it can be seen that the dipole moment of **G13** is relatively large (dipole moments of **G9**−**G11** molecules

https://doi.org/10.1021/acsomega.2c05466
ACS Omega 2022, 7, 39310−39324

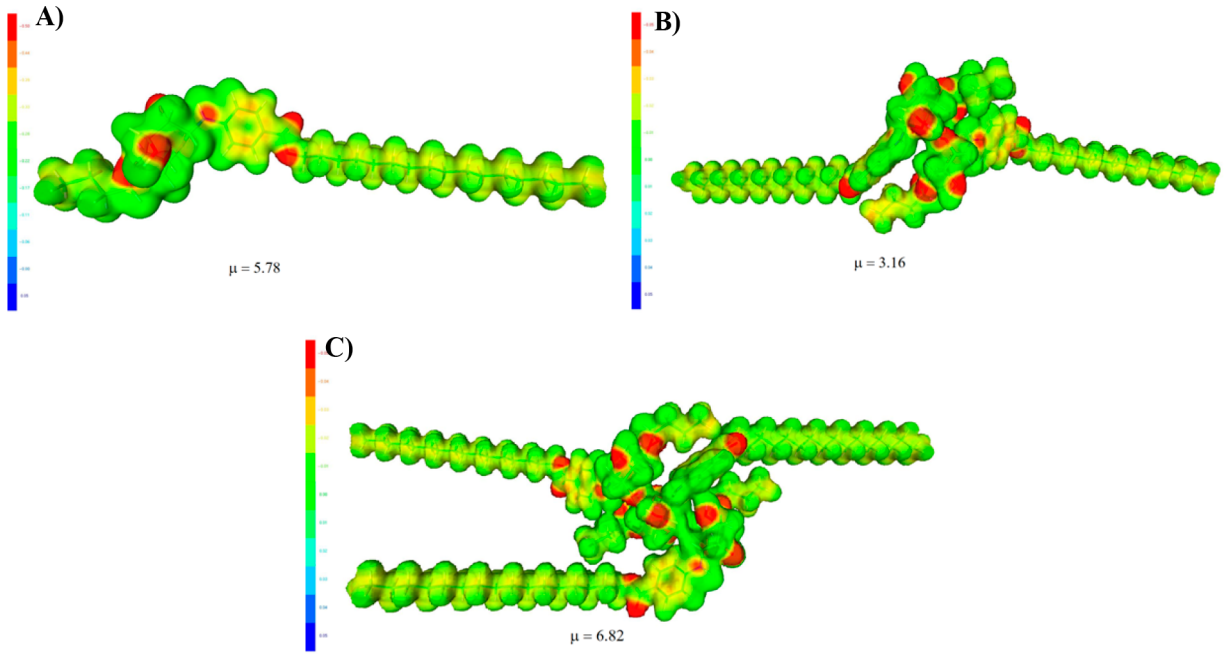

Figure 13. Plots of the electrostatic potential of (A) **G1** molecule, (B) **G1** dimer, and (C) trimer in ethanol solution (the dipole moments are in units of Debye).

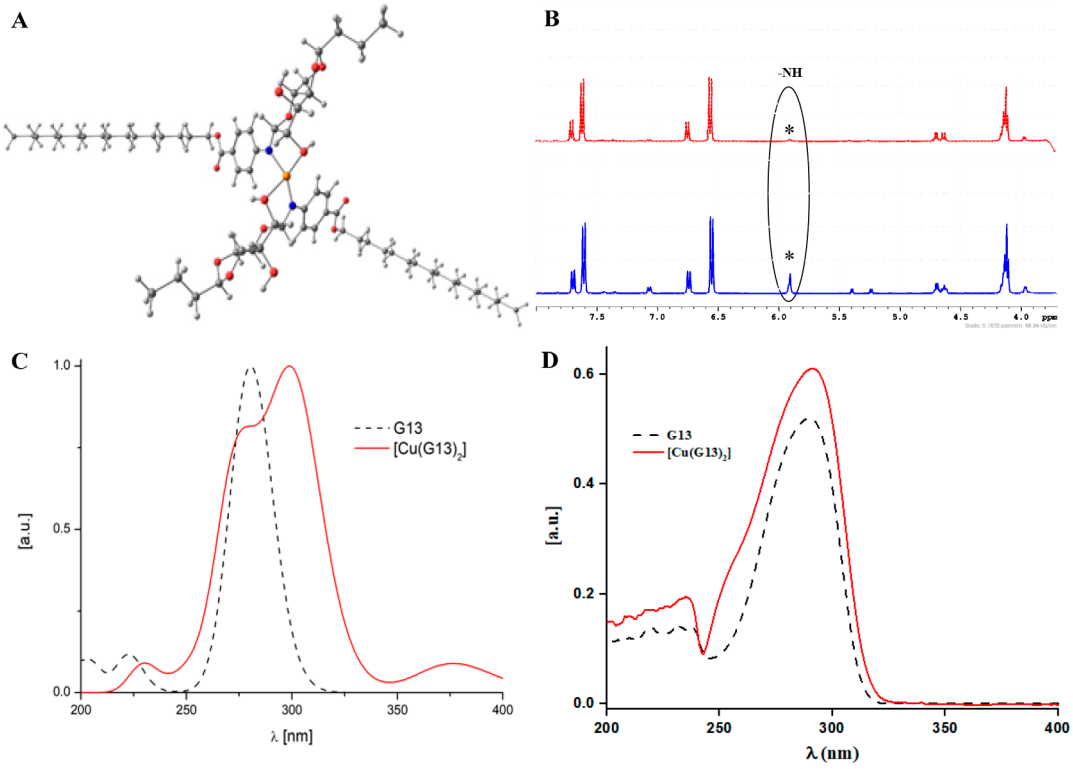

Figure 14. (A) Optimized structure of $[Cu(\mathbf{G13})_2]$, (B) partial NMR spectra of **G13** with Cu^{2+}, and (C,D) calculated and experimental absorption spectra of **G13** and $[Cu(\mathbf{G13})_2]$ respectively.

are similar, amounting to about 2.5 D, and μ of **G12** is 2.27 D), and the polar groups are evenly distributed around the cyclic part of the molecule. This is beneficial to the formation of solute−solvent hydrogen bonding interactions in solution. The magnitude of the dipole moments is enhanced from 4.49 D in the gas phase to 5.78 D in the ethanol solution. A similar increase in the dipole moment of the **G13** dimer can be seen when comparing the calculations in the gas phase with the ethanol solution (2.55 D in the gas phase and 3.16 D in the solution). On the other hand, the dipole moment of the **G13** dimer is reduced compared to that of the free molecule, which may suggest a reduction in gelling ability due to the dimerization of the compound. However, the calculated interaction energy of the dimer with another **G13** molecule

https://doi.org/10.1021/acsomega.2c05466
ACS Omega 2022, 7, 39310−39324

to form a trimer is significant and amounts to −16.94 kcal/mol. In addition, due to the shift of one of the molecules in the trimer, the dipole moment is much greater than that in the dimer, which favors the gelation ability.

To analyze the interaction between **G13** with Cu^{2+} ions, the geometry of the coordination compound [Cu(**G13**)$_2$], drawn in Figure 14A, was optimized at the same level as gelator molecules, and the NMR titration experiment was carried out to determine the role of the NH proton of glycosylamine in the binding of Cu^{2+} ions (Figure 14B). In the next step, the absorption spectrum using the time-dependent DFT method[63] was calculated. Figure 14C,D presents spectra of (theoretical and experimental) **G13** and [Cu(**G13**)$_2$], and there are visible significant hyperchromic and bathochromic effects for the band at about 300 nm. Using the counterpoise method, the binding **G13**···Cu^{2+} energy was estimated at −170.55 kcal/mol, which indicates the stability of the [Cu(**G13**)$_2$] complex (a possible mechanism for the selective detection of Cu^{2+} is given in Figure S14). The stability of the complex explains the transformation of the gel into sol after introducing Cu^{2+} ions into the system.

CONCLUSION

In conclusion, we have designed a series of alkyl-substituted sugar-aminobenzoate-based organogelators with outstanding rechargeability. *N*-Glycosylamine derivatives self-assemble to form a fibrous-like network, as confirmed using FE-SEM analysis. Among the six PSOGs, **G13** showed excellent properties. These organogelators show phase-selective gelation and can gelate various solvents from a solvent−water mixture at room temperature. Fascinatingly, the gelator was found to remove cationic dyes efficiently from its aqueous solution, signifying its substantial role in water purification. The gelator showed exceptional detection of Cu^{2+} ions by a change of state from gel−solution as compared to the other metal ions tested. Computational modeling provided atomic-scale insights into gel formation and the reason for the gel−sol transformation and stable [Cu(**G13**)] complex formation after the addition of Cu^{2+} metal ions.

EXPERIMENTAL SECTION

Materials. 4-Nitrobenzoyl chloride, 1-bromooctane, 1-bromododecane, 1-bromohexadecane, palladium−charcoal activated (10%), and crystal violet (CV) dye were bought from Sigma-Aldrich Pvt Ltd. USA and were high purity and used as received. D-Glucose, silica gel (100−200 mesh), paraldehyde, acetic anhydride, butyraldehyde, and solvents were purchased from SRL, India. The metal salts used for sensing studies were purchased from Alfa Aesar, India. The solvents used for the gelation studies were HPLC grade. TLC was performed using silica gel as an adsorbent and viewed through a UV chamber. Elution solvents used in TLC are chloroform and methanol.

*General Procedure for the Synthesis of Alkoxy Benzoate-Based N-Glycosylamines (**G8**−**G13**).* To a solution of alkyl-substituted aminobenzoate (**5**−**7**) (1.2 mmol) in dry ethanol was added and stirred 4,6-O-protected D-glycopyranoside (ethylidene and butylidene) (**a**, **b**) (1 mmol) for 6 h at room temperature. After completion of the reaction, the solvent was evaporated off under reduced pressure. The crude product was purified by column chromatography.

*Synthesis of N′-(4,6-O-Ethylidine-β-D-glucopyranosyl octyl)-Substituted Benzoate-Based N-Glycosylamine (**G8**).* Compound **G8** was obtained by the reaction of 4,6-*O*-ethylidine-β-D-glucopyranose (**a**) (1 mmol, 0.27 g) and octyl-substituted aminobenzoate (**5**) (1.2 mmol, 0.31 g) in ethanol as a colorless solid with 79% yield: mp 119−122 °C; ^{1}H NMR (500 MHz, $CDCl_3$ + DMSO-d_6, ppm) δ_H 7.82 (d, J = 6 Hz, 2H, Ar−H), 7.55 (d, J = 6 Hz, 2H, Ar−H), 6.05 (s, 1H, Sac-H), 5.80 (d, J = 3 Hz, 1H, Sac-H), 5.62 (s, 1H, Sac-H), 5.54−5.49 (m, 2H, Sac-H), 5.43 (t, J = 6 Hz, 2H, Sac-H), 4.98 (t, J = 3 Hz, 2H, −NCH_2), 4.84 (d, J = 3 Hz, 1H, Sac-H), 4.75 (t, J = 6 Hz,1H, Ano-H), 3.99 (m, 3H, Sac-H, −NH), 2.50 (t, J = 6 Hz, 2H, Ali-CH_2), 2.22−2.09 (m, 10H, Ali-CH_2), 1.68 (d, J = 6 Hz, Ali-CH_3); ^{13}C NMR (125 MHz, $CDCl_3$ + DMSO-d_6, ppm) δ_C 166.2, 151.4, 131.1, 118.8, 112.7, 99.1, 85.1, 80.7, 74.0, 74.0, 73.3, 70.1, 68.1, 67.0, 64.1, 62.2, 31.8, 29.5, 29.5, 29.5, 29.4, 29.2, 26.0, 22.6, 20.7, 14.3.

*Synthesis of N′-(4,6-O-Butylidine-β-D-glucopyranosyl octyl)-Substituted Benzoate-Based N-Glycosylamine (**G9**).* Compound **G9** was obtained by the reaction of 4,6-*O*-butylidine-β-D-glucopyranose (**b**) (1 mmol, 0.27 g) and octyl-substituted aminobenzoate (**6**) (1.2 mmol, 0.31 g) in ethanol as a colorless solid with 82% yield (0.46 g): mp 116−118 °C; ^{1}H NMR (500 MHz, $CDCl_3$ + DMSO-d_6, ppm) δ_H 7.54 (d, J = 6 Hz, 2H, Ar−H), 6.62−6.45 (d, J = 6 Hz, 2H, Ar−H), 5.95 (s, 1H, Sac-H), 4.87 (s, 2H, Sac-H), 4.34 (t, J = 6 Hz, 2H, Sac-H), 4.28−4.24 (m, 2H, Sac-H, −NH), 3.96−3.92 (dd, J = 3 Hz, 2H, Sac-H, −CH_2), 3.78−3.75 (m, 1H, Sac-H), 3.57 (t, J = 6 Hz, 1H, -Ano-H), 3.17−3.14 (m, 2H, Sac-H), 3.04 (s, 1H, Sac-H), 1.45 (t, J = 3 Hz, 2H, Ali-CH_2), 1.36−1.32 (m, 4H, Ali-CH_2), 1.31−1.12 (m, 8H, Protec-CH_3,Ali-CH_2), 1.00 (d, J = 3 Hz, 2H, Ali-CH_2), 0.60 (m, 6H, Ali-CH_3); ^{13}C NMR (125 MHz, $CDCl_3$ + DMSO-d_6, ppm) δ_C 166.2, 150.0, 131.2, 130.6, 129.4, 113.6, 112.9, 112.2, 101.7, 92.5, 80.4, 79.8, 73.3, 72.8, 70.0, 68.1, 61.7, 40.2, 35.7, 31.1, 28.6, 28.5, 28.1, 25.4, 22.0, 16.8, 13.5, 13.4.

*Synthesis of N′-(Acetyl-Protected 4,6-O-Butylidine-β-D-glucopyranosyl octyl)-Substituted Benzoate-Based N-Glycosylamine (**G10**).* Compound **G10** was obtained by the reaction of acetyl-protected 4,6-*O*-butylidine-β-D-glucopyranose (**c**) (1 mmol, 0.27 g) and octyl-substituted aminobenzoate (**5**) (1.2 mmol, 0.32 g) in ethanol as a colorless solid in 76% yield (0.46 g): mp 116−119 °C; ^{1}H NMR (300 MHz, $CDCl_3$ + DMSO-d_6, ppm) δ_H 7.85 (d, J = 8.4 Hz, 2H, Ar−H), 6.63 (d, J = 8.4 Hz, 2H, Ar−H), 5.73 (d, J = 8.1 Hz, 1H, Sac-H), 5.23 (d, J = 8.7 Hz, 1H, Sac-H), 5.07 (t, J = 9 Hz, 1H, Ano-H), 4.49 (t, J = 6 Hz, 1H, Sac-H), 4.24 (m, 3H, −CH_2, −NH), 3.49 (t, J = 6 Hz, 3H, Sac-H), 2.06 (t, J = 9 Hz, 6H, −OAc), 1.73 (t, J = 6.9 Hz, 2H, Ali-CH_2), 1.59 (t, J = 3 Hz, 2H, Ali-CH_2), 1.41−1.28 (m, 12H, −CH_2), 0.86 (t, J = 6 Hz, 6H, Ali-CH_3); ^{13}C NMR (75 MHz, $CDCl_3$ + DMSO-d_6, ppm) δ 170.0, 169.5, 168.8, 166.7, 150.7, 131.5, 120.1, 113.7, 102.6, 92.2, 71.8, 71.1, 67.8, 67.1, 64.5, 35.9, 31.7, 29.2, 29.1, 28.8, 26.6, 207, 20.6, 20.5, 17.3, 14.0, 13.7.

*Synthesis of N′-(4,6-O-Ethylidine-β-D-glucopyranosyl dodecyl)-Substituted Benzoate-Based N-Glycosylamine (**G11**).* Compound **G11** was obtained by the reaction of 4,6-*O*-ethylidine-β-D-glucopyranose (a) (1 mmol, 0.4 g) and dodecyl-substituted benzoate-based amine (**6**) (1.2 mmol, 0.42 g) in ethanol as a colorless solid in 68% yield (0.73 g): mp 116−119 °C; ^{1}H NMR (300 MHz, $CDCl_3$ + DMSO-d_6, ppm) δ_H 7.75 (d, J = 8.1 Hz, 2H, Ar−H), 6.63 (d, J = 8.4 Hz, 1H, Ar−H), 6.28 (s, 1H, Ar−H), 5.14 (s, 1H, Sac-H), 4.95 (s, 1H, Sac-H),

https://doi.org/10.1021/acsomega.2c05466
ACS Omega 2022, 7, 39310−39324

4.72 (d, J = 4.8 Hz, 2H, Sac-H), 4.60 (m, 1H, Sac-H), 4.20 (t, J = 3 Hz, 2H, $-CH_2$), 4.11−4.00 (m, 2H, Sac-H, −NH), 3.90−3.79 (m, 1H, Sac-H), 3.47 (t, J = 9.6 Hz, 3H, Ano-H, Sac-H), 1.71 (t, J = 3 Hz, 4H, Ali-CH_2), 1.34 (d, J = 4.8 Hz, 3H, Protec-CH_3), 1.25−120 (m, 20H, Ali-CH_2), 0.87 (t, J = 6. Hz, 3H, Alkyl-CH_3); ^{13}C NMR (75 MHz, $CDCl_3$ + DMSO-d_6, ppm) δ_C 166.2, 151.7, 130.8, 117.8, 112.8, 98.8, 97.0, 92.6, 80.5, 79.8, 75.5, 72.9, 70.1, 68.1, 67.7, 65.8, 63.6, 61.5, 31.3, 29.0, 28.9, 28.9, 28.7, 28.2, 25.5, 22.4, 20.2, 14.3; HR-MS (ESI) m/z calcd $[M + 2]^+$ 492.31123, found 494.31158.

*Synthesis of N′-(4,6-O-Butylidine-β-D-glucopyranosyl dodecyl)-Substituted Benzoate-Based N-Glycosylamine (**G12**).* Compound **G12** was obtained by the reaction of 4,6-*O*-butylidine-β-D-glucopyranose (b) (1 mmol, 0.27 g) and dodecyl-substituted aminobenzoate (**6**) (1.2 mmol, 0.31 g) in ethanol as a colorless solid in 71% (0.46 g) yield: mp 98−101 °C; ^{1}H NMR (300 MHz, $CDCl_3$ + DMSO-d_6, ppm) δ_H 7.78 (d, J = 8.1 Hz, 2H, Ar−H), 6.63 (d, J = 8.4 Hz, 1H, Ar−H), 6.20 (s, 1H, Ar−H), 5.16 (s, 1H, Sac-H), 4.76 (s, 1H, Sac-H), 4.55 (s, 2H, Sac-H), 4.38 (s, 1H, Sac-H), 4.22 (d, J = 6.0 Hz, 2H, $-NCH_2$), 4.13−4.03 (m, 1H, Sac-H, −NH), 3.85 (t, J = 9 Hz, 2H, Ano-H, Sac-H), 3.30−3.19 (m, 2H, Sac-H), 1.72−1.60 (m, 4H, Sac-CH_2), 1.46−1.413 (m, 4H, Ali-CH_2), 1.26−1.02 (m, 16H, Ali-CH_2), 0.96 (t, J = 5.7 Hz, 6H, Ali-CH_3); ^{13}C NMR (75 MHz, $CDCl_3$ + DMSO-d_6, ppm) δ_C 166.2, 151.3, 130.8, 118.2, 112.9, 101.7, 96.9, 92.5, 91.0, 80.4, 70.2, 68.2, 63.7, 61.7, 35.7, 31.3, 29.0, 28.9, 28.9, 28.7, 28.2, 25.5, 22.0, 16.6, 14,4; HRMS (ESI) m/z calcd 522.34253, found 522.34299.

*Synthesis of N′-(4,6-O-Ethylidene-β-D-glucopyranosyl hexadecyl)-Substituted Benzamide Based N-Glycosylamine (**G13**).* Compound **G13** was obtained by the reaction of 4,6-*O*-butylidine-β-D-glucopyranose (b) (1 mmol, 0.27 g) and hexadecyl-substituted aminobenzoate (7) (1.2 mmol, 0.32 g) in ethanol as a colorless solid in 66% (0.658 g) yield: mp 106−109 °C; ^{1}H NMR (300 MHz, $CDCl_3$ + DMSO-d_6, ppm) δ_H 7.82 (d, J = 8.4 Hz, 2H, Ar−H), 7.72 (d, J = 8.7 Hz, 2H, Ar−H), 6.29 (d, J = 6.6 Hz, 1H, - Ar−H), 5.13 (s, 1H, Sac-H), 4.92 (s, 1H, Sac-H), 4.73 (t, J = 5.4 Hz, 1H, Sac-H), 4.61 (t, J = 7.5 Hz, 1H, Sac-H), 4.21 (t, J = 6.6 Hz, 2H, Sac-H), 4.12 (m, 1H, −NH), 3.70 (t, J = 9 Hz, 1H, Ano-H), 3.54−3.40 (m, 4H, Sac-H), 3.34−3.25 (m, 2H, Sac-H), 1.72 (t, J = 7 Hz, 2H, $-CH_2$), 1.37−1.33 (t, J = 6 Hz, 9H, Ali-CH_3), 1.25 (m, 20H, $-CH_2$), 0.88 (d, J = 5.7 Hz, 6H, $-CH_3$); ^{13}C NMR (75 MHz, $CDCl_3$ + DMSO-d_6, ppm) δ_C 166.1, 150.0, 130.6, 119.4, 112.2, 98.9, 85.2, 80.5, 73.5, 73.3, 70.1, 67.7, 66.6, 63.8, 61.5, 31.3, 29.0, 29.0, 28.9, 28.7, 28.2, 25.5, 22.0, 19.9, 13.6; HR-MS (ESI) m/z calcd 550.37383, found 550.37353.

Stable-to-Inversion Method for Minimum Gelation Concentration (MGC) Determination. The MGCs of the gelators were determined using a dilution method. Ten milligrams of each gelator was added to 1 mL of solvent in a screw-capped glass vial and heated to obtain a homogeneous solution and cool it to room temperature. Then the formed gel system was gradually diluted with a particular volume of the tested solvent, and the heating−cooling procedure was repeated until no gel was formed. The final concentration at which the gel state remained with no flow observed after inverting the sample vial was recorded as the MGC value in the % w/v (mg/100 μL) unit.

Phase-Selective Gelation. Phase-selective gelation experiments were performed using petrol, kerosene, benzene oils (1 mL), and water (1.0 mL) in a ratio of 1:1. The gelator **G13** (3 mg) was added to a mixture of kerosene−water and benzene−water and dissolved upon heating. After being cooled to room temperature, gelation occurred while the aqueous phase remained intact. As shown in Figure 3, the gels are sufficiently firm to hold the water layer up. The oil layer was completely congealed within 5 min.

Dye Removal Experiment. Experiments were performed to investigate the absorption capability of synthesized PSGs toward CV from an aqueous solution. Different concentrations of CV (0.01−0.12 M) were prepared and mixed with the gel **G13** (benzene) sample (0.004 g, 0.01 mmol) separately. The plot of absorbance versus concentration of the dye solution was drawn according to the absorbance at 587 nm of the different dye concentrations at different time intervals (0−24 h) (Figure S4). The decrease in intensity of the peak occurs with time, which indicates the removal of CV from aqueous solution by superabsorbent PSG and becomes constant at equilibrium.

UV−Vis Titrations. **G13** (0.01 mmol) was dissolved in the ethanol−water solvent mixture (9:1, 10 mL), and 30 μL of it was diluted to 3 mL with the solvent mixture to make a final concentration of 10 μM. $Cu(NO_3)_2$ (0.1 mmol) was dissolved in 10 mL of triple distilled water, and 1.5−90 μL of the Cu^{2+} ion solution (10 mM) was transferred to the solution of **L** (10 μM) prepared above. After being mixed for a few seconds, UV−vis spectra were obtained at room temperature.

Job Plot Measurements. **G13** (0.01 mmol) was dissolved in ethanol (10 mL), and 100, 90, 80, 70, 60, 50, 40, 30, 20, 10, and 0 μL of the **L** solution was taken and transferred to the vials. Each vial was diluted with 2.9 mL of a mixed solvent. $Cu(NO_3)_2$ (0.01 mmol) was dissolved in triple distilled water (10 mL), and 0, 10, 20, 30, 40, 50, 60, 70, 80, 90, and 100 μL of the Cu^{2+} solution was added to each diluted **G13** solution. Each vial had a total volume of 3 mL. After being shaken for a minute, the absorbance spectra were obtained at room temperature.

Computational Studies. DFT calculations were performed in order to characterize the carbohydrate gelators and consider the simple dimeric model of the molecules. The analysis of the geometry of the dimer allowed us to estimate the strength of the intermolecular interactions responsible for the gel formation. Geometries of the compounds were optimized using the B3LYP functional[64,65] augmented with Grimme diffusion correction and GD3BJ[66] and 6-31G(d,p) basis sets.[67] The calculations were carried out with the Gaussian 16, revision C.01.[68] The continuum solvation model PCM[69] was used to describe the solvent (ethanol) effect. Based on the calculated geometries, the length of the molecules was determined.

■ ASSOCIATED CONTENT

Supporting Information

The Supporting Information is available free of charge at https://pubs.acs.org/doi/10.1021/acsomega.2c05466.

Synthetic scheme, FT-IR, ^{1}H NMR, ^{13}C NMR, HRMS, and characterization data for all compounds, photophysical data, Job's plot, detection limits, and computational studies assistant figures (PDF)

https://doi.org/10.1021/acsomega.2c05466
ACS Omega 2022, 7, 39310−39324

AUTHOR INFORMATION

Corresponding Author

Thangamuthu Mohan Das − *Department of Chemistry, School of Basic and Applied Sciences, Central University of Tamil Nadu (CUTN), Thiruvarur 610 005, India;* orcid.org/0000-0003-1217-334X; Phone: +91 9965048959; Email: tmohandas@cutn.ac.in, tmdas_72@yahoo.com

Authors

Panichiyil Valiyaveetil Bhavya − *Department of Chemistry, School of Basic and Applied Sciences, Central University of Tamil Nadu (CUTN), Thiruvarur 610 005, India*

Kamalakannan Soundarajan − *Department of Chemistry, School of Basic and Applied Sciences, Central University of Tamil Nadu (CUTN), Thiruvarur 610 005, India*

Jan Grzegorz Malecki − *Institute of Chemistry, University of Silesia, 40-006 Katowice, Poland*

Complete contact information is available at: https://pubs.acs.org/10.1021/acsomega.2c05466

Author Contributions

The manuscript was written through the contributions of all authors. All authors have given approval to the final version of the manuscript.

Notes

The authors declare no competing financial interest.

ACKNOWLEDGMENTS

T.M. thanks the Department of Chemistry, Central University of Tamil Nadu (CUTN), Thiruvarur, Tamil Nadu, for the infrastructure facility particularly NMR (400 MHz). P.V.B. and K.S. acknowledge CUTN for research fellowships. The Gaussian 09 calculations were carried out in the Wrocław Centre for Networking and Supercomputing, WCSS, Wrocław, Poland, http://www.wcss.wroc.pl (Grant No. 18).

REFERENCES

(1) Draper, E. R.; Adams, D. J. Controlling the Assembly and Properties of Low-Molecular-Weight Hydrogelators. *Langmuir* **2019**, *35*, 6506−6521.

(2) (a) Ono, F.; Ichimaru, K.; Hirata, O.; Shinkai, S.; Watanabe, H. Universal Glucose-based Low-molecular-weight Gelators for Both Organic and Aqueous Solvents. *Chem. Lett.* **2020**, *49*, 156−159. (b) Abdallah, D. J.; Weiss, R. G. Organogels and Low Molecular Mass Organic Gelators. *Adv. Mater.* **2000**, *12*, 1237−1247.

(3) (a) Morris, J.; Bietsch, J.; Bashaw, K.; Wang, G. Recently Developed Carbohydrate Based Gelators and Their Applications. *Gels* **2021**, *7*, 24−85. (b) Wang, J.; Kang, H.; Ma, H.; Liu, Y.; Xie, Z.; Wang, Y.; Fan, Z. Super-Fast Fabrication of MXene Film through a Combination of Ion Induced Gelation and Vacuum-Assisted Filtration. *Eng. Sci.* **2021**, *15*, 57−66. (c) Ul-Islam, M.; Ali, J.; Khan, W.; Haider, A.; Shah, N.; Md. Wasi, A.; Wajid Ullah, M.; Yang, G. Fast 4-nitrophenol Reduction Using Gelatin Hydrogel Containing Silver Nanoparticles. *Eng. Sci.* **2019**, *8*, 19−24. (d) Soares, S. F.; Fateixa, S.; Trindade, T.; Daniel-da-Silva, A. L. A Versatile Synthetic Route Towards Gelatin-silica Hybrids and Magnetic Composite Colloidal Nanoparticles. *Adv. Compos. Hybrid Mater.* **2022**, *5*, 884−898. (e) Hua, J.; Björling, M.; Larsson, R.; Shi, Y. Friction Control of Chitosan-Ag Hydrogel by Silver Ion. *ES Mater. Manuf.* **2022**, *16*, 30−36.

(4) (a) Arun, A.; Malrautu, P.; Laha, A.; Ramakrishna, S. Gelatin Nanofibers in Drug Delivery Systems and Tissue Engineering. *Eng. Sci.* **2021**, *16*, 71−81. (b) Bansode, N. D.; Sindhu, K. R.; Morel, C.; Rémy, M.; Verget, J.; Boiziau, C.; Barthélémy, P. Disulfide Based Low Molecular Weight Gel for the Selective Sustained Release of Biomolecules. *Biomater. Sci.* **2020**, *8*, 3186−3192.

(5) Brito, A.; Pereira, P.; Reis, R.; Ulijn, R.; Lewis, J. S.; Pires, R. A.; Pashkuleva, I. Aromatic Carbohydrate Amphiphile Disrupts Cancer Spheroids and Prevents Relapse. *Nanoscale* **2020**, *12*, 19088−19092.

(6) Sathyanarayanan, G.; Rodrigues, M.; Limon, D.; Rodriguez-Trujillo, R.; Puigmarti-Luis, J.; Perez-Garcia, L.; Amabilino, D. B. Drug-Loaded Supramolecular Gels Prepared in a Microfluidic Platform: Distinctive Rheology and Delivery through Controlled Far-from-Equilibrium Mixing. *ACS Omega* **2017**, *2*, 8849−8858.

(7) (a) Kartha, K. K.; Babu, S. S.; Srinivasan, S.; Ajayaghosh, A. Attogram Sensing of Trinitrotoluene with a Self-Assembled Molecular Gelator. *J. Am. Chem. Soc.* **2012**, *134*, 4834−4841. (b) Huang, H.; Han, L.; Wang, Y.; Yang, Z.; Zhu, F.; Xu, M. Tunable Thermal-Response Shape Memory Bio-Polymer Hydrogels as Body Motion Sensors. *Eng. Sci.* **2020**, *9*, 60−67.

(8) (a) Moradi, O.; Madanpisheh, M. A.; Moghaddas, M. Synthesis of GO/HEMA, GO/HEMA/TiO2, and GO/Fe3O4/HEMA as Novel Nanocomposites and their Dye Removal Ability. *Adv. Compos. Hybrid Mater.* **2021**, *4*, 1185−1204. (b) Aggrwal, G.; Salunke-Gawali, S.; Gejji, S. P.; Nikalje, M.; Chakravarty, D.; Verma, P. L.; Puranik, V. G. Reactions of 2,3-Dibromonaphthalene-1,4-Dione and Pyridyl Amines: X-ray Structures, DFT Investigations, and Selective Detection of the Hg2+ and Ni2+ Ions. *Eng. Sci.* **2021**, *14*, 78−93.

(9) (a) Mondal, S.; Bairi, P.; Das, S.; Nandi, A. K. Phase Selective Organogel from an Imine Based Gelator for Use in Oil Spill Recovery. *J. Mater. Chem. A* **2019**, *7*, 381−392. (b) Lim, J. Y. C.; Goh, S. S.; Liow, S. S.; Xue, K.; Loh, X. J. A Review of Bio-based Materials for Oil Spill Treatment. *J. Mater. Chem. A* **2019**, *7*, 18759−18791.

(10) Pathak, N. P.; Rajkamal; Yadav, S. A Gelator−starch Blend for Dry Powder Based Instant Solidification of Crude Oil at Room Temperature. *Chem. Commun.* **2020**, *56*, 2999−3002.

(11) Vibhute, A. M.; Sureshan, K. M. How Far Are We in Combating Marine Oil Spills by Using Phase-Selective Organogelators? *Chem. Sus. Chem.* **2020**, *13*, 5343−5360.

(12) (a) Ramalingam, S.; Subramania, A. Effective Removal of Nitrates from the Drinking Water by Chemical and Electrochemical Methods. *Eng. Sci.* **2021**, *15*, 80−88. (b) Okesola, B. O.; Smith, D. K. Applying Low-molecular Weight Supramolecular Gelators in an Environmental Setting—Self-assembled Gels as Smart Materials for Pollutant Removal. *Chem. Soc. Rev.* **2016**, *45*, 4226−4251. (c) Ahmadi, S. A. R.; Kalaee, M. R.; Moradi, O.; Nosratinia, F.; Abdouss, M. Core−shell Activated Carbon-ZIF-8 Nanomaterials for the Removal of Tetracycline from Polluted Aqueous Solution. *Adv. Compos. Hybrid Mater.* **2021**, *4*, 1384−1397.

(13) (a) Narayana, C.; Kumari, P.; Tiwari, G.; Sagar, R. Triazole Linked N-Acetylglucosamine Based Gelators for Crude Oil Separation and Dye Removal. *Langmuir* **2019**, *35*, 16803−16812. (b) Sun, Z.; Qu, K.; Cheng, Y.; You, Y.; Huang, Z.; Umar, A.; Ibrahim, Y. S.; Algadi, H.; Castañeda, L.; Colorado, H. A.; Guo, Z. Corncob-derived Activated Carbon for Efficient Adsorption Dye in Sewage. *ES Food & Agroforestry* **2021**, *4*, 61−73. (c) Kumar, R.; Umar, A.; Kumar, R.; Chauhan, M. S.; Kumar, G.; Chauhan, S. Spindle-like Co_3O_4-ZnO Nanocomposites Scaffold for Hydrazine Sensing and Photocatalytic Degradation of Rhodamine B Dye. *Eng. Sci.* **2021**, *16*, 288−300.

(14) (a) Shinde, D. R.; Quraishi, I. S.; Pawar, R. A. An Efficient Visible Light Driven Photocatalytic Removal of Dyes from the Dye Effluent using Metal Halide Lamp Based Slurry Reactor. *ES Energy & Environ.* **2021**, *14*, 54−62. (b) Fan, T.; Deng, W.; Gang, Y.; Du, Z.; Li, Y. Degradation of Hazardous Organics via Cathodic Flow-through Process Using a Spinel $FeCo_2O_4$/CNT Decorated Stainless-Steel Mesh. *ES Mater. Manuf.* **2021**, *12*, 53−62. (c) Kumar, S. A.; Jarvin, M.; Sharma, S.; Umar, A.; Inbanathan, S. S. R.; Lalla, N. P. Facile and Green Synthesis of MgO Nanoparticles for the Degradation of Victoria Blue Dye under UV Irradiation and their Antibacterial Activity. *ES Food & Agroforestry* **2021**, *5*, 14−19.

(15) Raza, R.; Panja, A.; Ghosh, K. Diaminomaleonitrile-functionalized Gelators in F−/CN− Sensing, Phase-selective Gelation, Oil

https://doi.org/10.1021/acsomega.2c05466
ACS Omega 2022, 7, 39310−39324

Spill Recovery and Dye Removal from Water. *New J. Chem.* **2020**, *44*, 10275−10285.
(16) Ramos, J.; Arufe, S.; Martin, H.; Rooney, D. A.; Elmes, R. B. P.; Erxleben, A.; Moreira, R.; Velasco-Torrijos, T. Glycosyl Squaramides, a New Class of Supramolecular Gelators. *Soft Matter* **2020**, *16*, 7916−7926.
(17) Liu, M.; Ouyang, G. H.; Niu, D.; Sang, Y. Supramolecular Gelatons: Towards the Design of Molecular Gels. *Org. Chem. Front.* **2018**, *5*, 2885−2900.
(18) (a) Hoque, J.; Sangaj, N.; Varghese, S. Stimuli-Responsive Supramolecular Hydrogels and Their Applications in Regenerative Medicine. *Macromol. Biosci.* **2018**, *19*, No. e1800259. (b) Xia, X.; Xu, X.; Lin, C.; Yang, Y.; Zeng, L.; Zheng, Y.; Wu, X.; Li, W.; Xiao, L.; Qian, Q.; Chen, Q. Microalgal-immobilized Biocomposite Scaffold Fabricated by Fused Deposition Modeling 3D Printing Technology for Dyes Removal. *ES Mater. Manuf.* **2020**, *7*, 40−50.
(19) (a) Wang, D.; Chen, A.; Morris, J.; Wang, G. Stimuli-responsive Gelators from Carbamoyl Sugar Derivatives and their Responses to Metal Ions and Tetrabutylammonium Salts. *RSC Adv.* **2020**, *10*, 40068−40083. (b) Gijare, M.; Chaudhari, S.; Ekar, S.; Garje, A. Reduced Graphene Oxide Based Electrochemical Nonenzymatic Human Serum Glucose Sensor. *ES Mater. Manuf.* **2021**, *14*, 110−119.
(20) (a) Khayat, Z.; Zali-Boeini, H. Novel Sugar-based Azo Dyes as Multistimuli Responsive Supramolecular Gelators and Chemosensors. *Dye. Pigment.* **2018**, *159*, 337−344. (b) Li, Y.; Guo, J.; Li, M.; Tang, Y.; Murugadoss, V.; Seok, I.; Yu, J.; Sun, L.; Sun, C.; Luo, Y. Recent Application of Cellulose Gel in Flexible Sensing-A Review. *ES Food & Agroforestry* **2021**, *4*, 9−27.
(21) Panja, S.; Mondal, S.; Ghosh, S.; Ghosh, U.; Ghosh, K. Effect of Substitution at Amine Functionality of 2,6-Diaminopyridine-Coupled Rhodamine on Metal-Ion Interaction and Self-Assembly. *ACS Omega* **2020**, *5*, 13984−13993.
(22) Zhang, Y. M.; Zhu, W.; Qu, W. J.; Zhong, K. P.; Chen, X. P.; Yao, H.; Wei, T. B.; Lin, Q. Competition of Cation−π and Exo-wall π−π Interactions: A Novel Approach to Achieve Ultrasensitive Response. *Chem. Commun.* **2018**, *54*, 4549−4552.
(23) Morris, J.; Bietsch, J.; Bashaw, K.; Wang, G. Recently Developed Carbohydrate Based Gelators and Their Applications. *Gels* **2021**, *7*, 24.
(24) Feng, X.; Luo, Y.; Li, F.; Jian, X.; Liu, Y. Development of Natural-Drugs-Based Low-Molecular-Weight Supramolecular Gels. *Gels* **2021**, *7*, 105.
(25) Sharma, P.; Wang, G. 4, 6-O-Phenylethylidene Acetal Protected D-Glucosamine Carbamate-Based Gelators and Their Applications for Multi-Component Gels. *Gels* **2022**, *8*, 191.
(26) Wang, Y.; Yu, X.; Fan, W.; Liu, R.; Liu, Y. Alginate-Oil Gelator Composite Foam for Effective Oil Spill Treatment. *Carbohydr. Polym.* **2022**, *294*, 119755.
(27) Fan, K.; Wang, X.; Wang, X.; Yang, H.; Han, G.; Zhou, L.; Fang, S. One-step-synthesized D-gluconic Acetal-based Supramolecular Organogelators with Effective Phase-selective Gelation. *RSC Adv.* **2020**, *10*, 37080−37085.
(28) Li, J.; Wei, H.; Peng, Y.; Geng, L.; Zhu, L.; Cao, X. Y.; Liu, C. S.; Pang, H. A Multifunctional Self-healing G-PyB/KCl Hydrogel: Smart Conductive, Rapid Room-temperature Phase-selective Gelation, and Ultrasensitive Detection of Alpha-fetoprotein. *Chem. Commun.* **2019**, *55*, 7922−7925.
(29) (a) Kumar, R.; Umar, A.; Kumar, R.; Chauhan, M. S.; Kumar, G.; Chauhan, S. Spindle-like Co3O4-ZnO Nanocomposites Scaffold for Hydrazine Sensing and Photocatalytic Degradation of Rhodamine B Dye. *Eng. Sci.* **2021**, *16*, 288−300. (b) Yu, M.; Yu, T.; Chen, S.; Guo, Z.; Seok, I. A Facile Synthesis of Ag/TiO_2/rGO Nanocomposites with Enhanced Visible Light Photocatalytic Activity. *ES Mater. Manuf.* **2020**, *7*, 64−69. (c) Zhang, F.; Cheng, W.; Yu, Z.; Ge, S.; Shao, Q.; Pan, D.; Liu, B.; Wang, X.; Guo, Z. Microwave Hydrothermally Synthesized WO3/UiO-66 Nanocomposites Toward Enhanced Photocatalytic Degradation of Rhodamine B. *Adv. Compos. Hybrid Mater.* **2021**, *4*, 1330−1342.
(30) (a) Li, W.; Zhou, L.; Xie, L.; Kang, K.; Xu, J.; Chai, X. N-Fe-Gd co-doped TiO2/g-C3N4 Nanosheet Hybrid Composites with Superior Photocatalytic Dye Degradation. *Adv. Compos. Hybrid Mater.* **2022**, *5*, 481−490. (b) Lin, C.; Liu, B.; Pu, L.; Sun, Y.; Xue, Y.; Chang, M.; Li, X.; Lu, X.; Chen, R.; Zhang, J. Photocatalytic Oxidation Removal of Fluoride Ion in Wastewater by g-C3N4/TiO2 Under Simulated Visible Light. *Adv. Compos. Hybrid Mater.* **2021**, *4*, 339−349. (c) Ali Baig, A. B.; Rathinam, V.; Ramya, V. Facile Fabrication of Zn-doped SnO2 Nanoparticles for Enhanced Photocatalytic Dye Degradation Performance Under Visible Light Exposure. *Adv. Compos. Hybrid Mater.* **2021**, *4*, 114−126.
(31) (a) Ali Baig, A. B.; Rathinam, V.; Ramya, V. Facile Fabrication of Zn-Doped SnO_2 Nanoparticles for Enhanced Photocatalytic Dye Degradation Performance Under Visible Light Exposure. *Adv. Compos. Hybrid Mater.* **2021**, *4*, 114−26. (b) Jing, C.; Zhang, Y.; Zheng, J.; Ge, S.; Lin, J.; Pan, D.; Naik, N.; Guo, Z. In-Situ Constructing Visible Light CdS/Cd-MOF Photocatalyst with Enhanced Photodegradation of Methylene Blue. *Particuology* **2022**, *69*, 111−122. (c) Kumar, R.; Umar, A.; Kumar, R.; Chauhan, M. S.; Kumar, G.; Chauhan, S. Spindle-Like Co_3O_4-ZnO Nanocomposites Scaffold for Hydrazine Sensing and Photocatalytic Degradation of Rhodamine B dye. *Eng. Sci.* **2021**, *16*, 288−300.
(32) Zhang, Y.; Zheng, J.; Nan, J.; Gai, C.; Shao, Q.; Murugadoss, V.; Maganti, S.; Naik, N.; Algadi, H.; Huang, M.; Xu, B. B.; Guo, Z. Influence of mass ratio and calcination temperature on physical and photoelectrochemical properties of ZnFe-layered double oxide/cobalt oxide heterojunction semiconductor for dye degradation applications. *Particuology* **2023**, *74*, 141−155.
(33) Rajput, R. B.; Jamble, S. N.; Kale, R. B. Solvothermal Synthesis of Anatase TiO_2 for the Detoxification of Methyl Orange Dye with Improved Photodegradation Efficiency. *Eng. Sci.* **2021**, *17*, 176−184.
(34) Nandanwar, R.; Bamne, J.; Singh, N.; Sharma, P. K.; Singh, P.; Umar, A.; Haque, F. Z. Synthesis of Titania/Silica Nanocomposite for Enhanced Photodegradation of Methylene Blue and Methyl Orange Dyes Under UV and Mercury Lights. *ES Mater. Manuf.* **2022**, *16*, 78−88.
(35) Jain, B.; Singh, A. K.; Hashmi, A.; Susan, Md. A. B. H.; Lellouche, J.-P. Surfactant-assisted cerium oxide and its catalytic activity towards Fenton process for non-degradable dye. *Adv. Compos. Hybrid Mater.* **2020**, *3*, 430−441.
(36) Sun, Z.; Zhang, Y.; Guo, S.; Shi, J.; Shi, C.; Qu, K.; Qi, H.; Huang, Z.; Murugadoss, V.; Huang, M.; Guo, Z. Confining FeNi nanoparticles in biomass-derived carbon for effectively photo-Fenton catalytic reaction for polluted water treatment. *Adv. Compos. Hybrid Mater.* **2022**, *5*, 1566−1581.
(37) Si, Y.; Li, J.; Cui, B.; Tang, D.; Yang, L.; Murugadoss, V.; Maganti, S.; Huang, M.; Guo, Z. Janus phenol−formaldehyde resin and periodic mesoporous organic silica nanoadsorbent for the removal of heavy metal ions and organic dyes from polluted water. *Adv. Compos. Hybrid Mater.* **2022**, *5*, 1180−1195.
(38) (a) Kumar, S. A.; Jarvin, M.; Sharma, S.; Umar, A.; Inbanathan, S. S.; Lalla, N. P. Facile and green synthesis of MgO nanoparticles for the degradation of victoria blue dye under UV irradiation and their antibacterial activity. *ES Food & Agroforestry* **2021**, *5*, 14−29. (b) Jadhav, P.; Shinde, S.; Suryawanshi, S. S.; Teli, B.; Patil, P. S.; Ramteke, A. A.; Hiremath, N. G.; Prasad, N. R. Green AgNPs decorated ZnO nanocomposites for dye degradation and antimicrobial applications. *Eng. Sci.* **2020**, *12*, 79−94. (c) Cheng, M.; Yao, C.; Su, Y.; Liu, J.; Xu, L.; Bu, J.; Wang, H.; Hou, S. Cyclodextrin modified graphene membrane for highly selective adsorption of organic dyes and copper (II) ions. *Eng. Sci.* **2022**, *18*, 299−307.
(39) (a) Singh, N.; Jana, S.; Singh, G. P.; Dey, R. K. Graphene-supported TiO2: study of promotion of charge carrier in photocatalytic water splitting and methylene blue dye degradation. *Adv. Compos. Hybrid Mater.* **2020**, *3*, 127−140. (b) Moradi, O.; Madanpisheh, M. A.; Moghaddas, M. Synthesis of GO/HEMA, GO/HEMA/TiO2, and GO/Fe3O4/HEMA as novel nanocomposites and their dye removal ability. *Adv. Compos. Hybrid Mater.* **2021**, *4*, 1185−204.

https://doi.org/10.1021/acsomega.2c05466
ACS Omega 2022, 7, 39310−39324

(40) Sun, Z.; Qu, K.; Cheng, Y.; You, Y.; Huang, Z.; Umar, A.; Ibrahim, Y. S.; Algadi, H.; Castañeda, L.; Colorado, H. A.; Guo, Z. Corncob-derived activated carbon for efficient adsorption dye in sewage. *ES Food & Agroforestry* **2021**, *4*, 61−73.
(41) Sun, Z.; Qu, K.; Li, J.; Yang, S.; Yuan, B.; Huang, Z.; Guo, Z. Self-template biomass-derived nitrogen and oxygen co-doped porous carbon for symmetrical supercapacitor and dye adsorption. *Adv. Compos. Hybrid Mater.* **2021**, *4*, 1413−24.
(42) Xia, X.; Xu, X.; Lin, C.; Yang, Y.; Zeng, L.; Zheng, Y.; Wu, X.; Li, W.; Xiao, L.; Qian, Q.; Chen, Q. Microalgal-immobilized biocomposite scaffold fabricated by fused deposition modeling 3D printing technology for dyes removal. *ES Materials & Manuf.* **2020**, *8*, 40−50.
(43) Zhang, F.; Lian, M.; Alhadhrami, A.; Huang, M.; Li, B.; Mersal, G. A.; Ibrahim, M. M.; Xu, M. Laccase immobilized on functionalized cellulose nanofiber/alginate composite hydrogel for efficient bisphenol A degradation from polluted water. *Adv. Compos. Hybrid Mater.* **2022**, *5*, 1852.
(44) Liao, Y.; Wang, Y.; Ouyang, L.; Dong, Y.; Zhou, J.; Hu, Q.; Qiu, B. Conductive polyaniline enhanced decolorization of azo dyes in anaerobic wastewater treatment. *ES Food & Agroforestry* **2021**, *6*, 35−42.
(45) Bhattacharya, S.; Krishnan-Ghosh, Y. First Report of Phase Selective Gelation of Oil from Oil/Water Mixtures. Possible Implications Toward Containing Oil Spills. *Chem. Commun.* **2001**, 185−186.
(46) (a) Rohilla, D.; Chaudhary, S.; Umar, A. An overview of advanced nanomaterials for sensor applications. *Eng. Sci.* **2021**, *16*, 47−70. (b) Kumar, R.; Umar, A.; Kumar, R.; Chauhan, M. S.; Kumar, G.; Chauhan, S. Spindle-like Co_3O_4-ZnO nanocomposites scaffold for hydrazine sensing and photocatalytic degradation of rhodamine B dye. *Eng. Sci.* **2021**, *16*, 288−300. (c) Vijeata, A.; Chaudhary, G. R.; Umar, A.; Chaudhary, S. Distinctive solvatochromic response of fluorescent carbon dots derived from different components of Aegle Marmelos plant. *Eng. Sci.* **2021**, *15*, 197−209.
(47) (a) Kumari, M.; Chaudhary, G. R.; Chaudhary, S.; Umar, A. Rapid analysis of trace sulphite ion using fluorescent carbon dots produced from single use plastic cups. *Eng. Sci.* **2021**, *17*, 101−112. (b) Jayachandiran, J.; Arivanandhan, M.; Padmaraj, O.; Jayavel, R.; Nedumaran, D. Investigation on ozone-sensing characteristics of surface sensitive hybrid rGO/WO_3 nanocomposite films at ambient temperature. *Adv. Compos. Hybrid Mater.* **2020**, *3*, 16−30. (c) Umar, A.; Kumar, R.; Algadi, H.; Ahmed, J.; Jalalah, M.; Ibrahim, A. A.; Harraz, F. A.; Alsaiari, M. A.; Albargi, H. Highly sensitive and selective 2-nitroaniline chemical sensor based on Ce-doped SnO2 nanosheets/Nafion-modified glassy carbon electrode. *Adv. Compos. Hybrid Mater.* **2021**, *4*, 1015−26.
(48) Zhu, H.; Fan, J.; Wang, B. H.; Peng, X. J. Fluorescent, MRI, and Colorimetric Chemical Sensors for the First-row d-block Metal Ions. *Chem. Soc. Rev.* **2015**, *44*, 4337−4366.
(49) Sekhar, K. P. C.; Swain, D. K.; Holey, S. A.; Bojja, S.; Nayak, R. R. Impact of Glycolipids Hydrophobic Chain Length, Headgroup Size on Self Assembly and Hydrophobic Guest Release. *Langmuir* **2020**, *36*, 3080−3088.
(50) Bull, P. C.; Thomas, G. R.; Rommens, J. M.; Forbes, J. R.; Cox, D. W. The Wilson Disease Gene is a Putative Copper Transporting P-type ATPase Similar to the Menkes Gene. *Nat. Genet.* **1993**, *5*, 327−337.
(51) Blackburn, O. A.; Coe, B. J.; Fielden, J.; Helliwell, M.; McDouall, J. J. W.; Hutchings, M. G. Nickel(II) and Palladium(II) Complexes of Azobenzene-containing Ligands as Dichroic Dyes. *Inorg. Chem.* **2010**, *49*, 9136−9150.
(52) Soundarajan, K.; Das, T. M. Sugar-benzohydrazide Based Phase Selective Gelators for Marine Oil Spill Recovery and Removal of Dye from Polluted Water. *Carbohydr. Res.* **2019**, *48*, 160−166.
(53) Pal, K. B.; Mukhopadhyay, B. Carbohydrate-Based Safe Fuel Gel with Significant Self−healing Property. *Chemistry Select* **2017**, *2*, 967−974.
(54) Singh, W. P.; Singh, R. S. A New Class of Organogelators Based on Triphenylmethyl Derivatives of Primary Alcohols: Hydrophobic Interactions Alone can Mediate Gelation. *Beilstein J. Org. Chem.* **2017**, *13*, 138−149.
(55) Kulkarni, M. R.; Revanth, T.; Acharya, A.; Bhat, P. Removal of Crystal Violet Dye from Aqueous Solution Using Water Hyacinth: Equilibrium, Kinetics and Thermodynamics Study. *Resource-Efficient Technologies* **2017**, *3*, 71−77.
(56) (a) Chen, J.; Wang, X.; Huang, Y.; Lv, S.; Cao, X.; Yun, J.; Cao, D. Adsorption Removal of Pollutant Dyes in Wastewater by Nitrogen-doped Porous Carbons Derived from Natural Leaves. *Eng. Sci.* **2019**, *5*, 30−38. (b) Gu, H.; Gao, C.; Zhou, X.; Du, A.; Naik, N.; Guo, Z. Nanocellulose Nanocomposite Aerogel Towards Efficient Oil and Organic Solvent Adsorption. *Adv. Compos. Hybrid Mater.* **2021**, *4*, 459−468. (c) Guo, L.; Zhang, Y.; Zheng, J.; Shang, L.; Shi, Y.; Wu, Q.; Liu, X.; Wang, Y.; Shi, L.; Shao, Q. Synthesis and Characterization of ZnNiCr-layered Double Hydroxides with High Adsorption Activities for Cr(VI). *Adv. Compos. Hybrid Mater.* **2021**, *4*, 819−829.
(57) Rehman, T. U.; Bibi, S.; Khan, M.; Ali, I.; Shah, L. A.; Khan, A.; Ateeq, M. Fabrication of Stable Superabsorbent Hydrogels for Successful Removal of Crystal Violet from Waste Water. *RSC Adv.* **2019**, *9*, 40051−40061.
(58) (a) Enenebeaku, C. K.; Okorocha, N. J.; Enenebeaku, U. E.; Onyeachu, B. I. Removal of Crystal Violet Dye by Adsorption onto Picrilima Nitida Stem Bark Powder: Kinetics and Isotherm Studies. *IOSR-JAC* **2016**, *9*, 14−23. (b) Bhorde, A.; Waykar, R.; Rondiya, S. R.; Nair, S.; Lonkar, G.; Funde, A.; Dzade, N. Y.; Jadkar, S. Structural, Electronic, and Optical Properties of Lead-Free Halide Double Perovskite Rb2AgBiI6: A Combined Experimental and DFT Study. *ES Mater. Manuf.* **2021**, *12*, 43−52.
(59) (a) Shetty, D. K.; Rodrigues, L. L.; Shetty, A. K.; Nair, G. Machine Learning based Predictors of Cardiovascular Disease among Young Adults. *Eng. Sci.* **2022**, *17*, 292−302. (b) Balakrishnan, A.; Medikonda, J.; Namboothiri, P. K. Role of Wearable Sensors with Machine Learning Approaches in Gait Analysis for Parkinson's Disease Assessment: A Review. *Eng. Sci.* **2022**, *19*, 5−19. (c) Rane, P. R.; Vincent, S. Landslide Susceptibility Mapping Using Machine Learning Algorithms for Nainital, India. *Eng. Sci.* **2021**, *17*, 142−155.
(60) (a) Chadaga, K.; Prabhu, S.; Umakanth, S.; Bhat, K.; Sampathila, N.; Chadaga, R. COVID-19 mortality prediction among patients using epidemiological parameters: an ensemble machine learning approach. *Eng. Sci.* **2021**, *16*, 221−233. (b) Wang, Y.; Peng, G.; Sharshir, S. W.; Yang, N. The weighted values of solar evaporation's environment factors obtained by machine learning. *ES Materials & Manuf.* **2021**, *14*, 87−94. (c) Han, G.; Sun, Y.; Feng, Y.; Lin, G.; Lu, N. Machine learning regression guided thermoelectric materials discovery−a review. *ES Materials & Manuf.* **2021**, *14*, 20−35. (d) He, Z.; Yang, M.; Wang, L.; Bao, E.; Zhang, H. Concentrated photovoltaic thermoelectric hybrid system: an experimental and machine learning study. *Eng. Sci.* **2021**, *15*, 47−56.
(61) (a) Joshi, S. C. Knowledge based data boosting exposition on CNT-engineered carbon composites for machine learning. *Advanced Composites and Hybrid Materials* **2020**, *3*, 354−64. (b) Chen, L.; Lan, C.; Xu, B.; Bi, K. Progress on material characterization methods under big data environment. *Advanced Composites and Hybrid Materials.* **2021**, *4*, 235−247. (c) Hou, H.; Pan, Y.; Bai, G.; Li, Y.; Murugadoss, V.; Zhao, Y. High-throughput computing for hydrogen transport properties in ε-ZrH2. *Adv. Compos. Hybrid Mater.* **2022**, *5*, 1350−1361.
(62) Boys, S. F.; Bernardi, F. The Calculation of Small Molecular Interactions by the Differences of Separate Total Energies. Some Procedures with Reduced Errors. *Mol. Phys.* **1970**, *19*, 553−566.
(63) Casida, M. E.; Jamorski, C.; Casida, K. C.; Salahub, D. R. Molecular Excitation Energies to High-Lying Bound States from Time-Dependent Density-Functional Response Theory: Characterization and Correction of the Time-Dependent Local Density Approximation Ionization Threshold. *J. Chem. Phys.* **1998**, *108*, 4439.

https://doi.org/10.1021/acsomega.2c05466
ACS Omega 2022, 7, 39310−39324

(64) Becke, A. D. Density-Functional Exchange-Energy Approximation with Correct Asymptotic Behavior. *Phys. Rev. A* **1988**, *38*, 3098.
(65) Perdew, J. P. Density-Functional Approximation for the Correlation Energy of the Inhomogeneous Electron Gas. *Phys. Rev. B* **1986**, *33*, 8822.
(66) Grimme, S.; Ehrlich, S.; Goerigk, L. Effect of the Damping Function in Dispersion Corrected Density Functional Theory. *J. Comput. Chem.* **2011**, *32*, 1456−1465.
(67) Ditchfield, R.; Hehre, W. J.; Pople, J. A. Self-Consistent Molecular-Orbital Methods. IX. An Extended Gaussian-Type Basis for Molecular-orbital Studies of Organic Molecules. *J. Chem. Phys.* **1971**, *54*, 724−728.
(68) Frisch, M. J.; Trucks, G. W.; Schlegel, H. B.; Scuseria, G. E.; Robb, M. A; Cheeseman, J. R.; Scalmani, G.; Barone, V.; Petersson, G A.; Nakatsuji, H.; Li, X.; Caricato, M.; Marenich, A. V.; Bloino, J.; Janesko, B. G.; Gomperts, R.; Mennucci, H. P.; Hratchian, J. V.; Ortiz, A. F; Izmaylov, J. L; Sonnenberg, D.; Williams-Young, B.; Ding, F.; Lipparini, F.; Egidi, F.; Goings, J.; Peng, B.; Petrone, A.; Henderson, T.; Ranasinghe, D.; Zakrzewski, V. G.; Gao, J.; Rega, N.; Zheng, G.; Liang, W.; Hada, M.; Ehara, M.; Toyota, K.; Fukuda, R.; Hasegawa, J.; Ishida, M.; Nakajima, T.; Honda, Y.; Kitao, O.; Nakai, H.; Vreven, T.; Throssell, K.; Montgomery, J. A., Jr.; Peralta, J. E.; Ogliaro, F.; Bearpark, M. J.; Heyd, J. J.; Brothers, E. N.; Kudin, K. N.; Staroverov, V. N.; Keith, T. A.; Kobayashi, R.; Normand, J.; Raghavachari, K.; Rendell, A. P.; Burant, J. C.; Iyengar, S. S.; Tomasi, J.; Cossi, M.; Millam, J. M.; Klene, M.; Adamo, C.; Cammi, R.; Ochterski, J. W.; Martin, R. L.; Morokuma, K.; Farkas, O.; Foresman, J. B; Fox, D. J. *Gaussian 16*, revision C.01; Gaussian, Inc.: Wallingford, CT, 2019.
(69) Barone, V.; Cossi, M. Quantum Calculation of Molecular Energies and Energy Gradients in Solution by a Conductor Solvent Model. *J. Phys. Chem. A* **1998**, *102*, 1995−2001.

https://doi.org/10.1021/acsomega.2c05466
ACS Omega 2022, 7, 39310−39324